Sea surface acidification events in the Andaman Sea associated with the last Toba volcanic activity

Ana Alves, Matthieu Paulhac Buisson, Pascale Louvat, Claire Rollion-Bard, Franck Bassinot, William Robert Gray, Guillaume Paris, Benoît Caron, Giulia Del Manzo, Anne Le Friant, et al.

Title

Sea surface acidification events in the Andaman Sea associated with the last Toba volcanic activity

Authors names

Ana Alves[a*], Matthieu Paulhac Buisson[b], Pascale Louvat[c], Claire Rollion-Bard[d], Franck Bassinot[d], William R. Gray[d], Guillaume Paris[e], Benoit Caron[f], Giulia Del Manzo[b], Anne Le Friant[b], Eva Moreno[g] and Annachiara Bartolini[a]

Authors Affiliations

a. Centre de Recherche en Paléontologie - Paris, UMR 7207, Muséum National d'Histoire Naturelle, CNRS, Sorbonne Université, 75005 Paris, France.
b. Université Paris Cité, Institut de physique du globe de Paris, CNRS, 75005 Paris, France.
c. Institut des Sciences Analytiques et de Physico-Chimie pour l'Environnement et les Matériaux, UMR 5254, CNRS, Université de Pau et des Pays de l'Adour, 64053 Pau, France.
d. Laboratoire des Sciences du Climat et de l'Environnement LSCE/IPSL, UMR 8212, CEA-CNRS-UVSQ, 91191 Gif-sur-Yvette, France.
e. Université de Lorraine – CNRS, Centre de Recherches Pétrographiques et Géochimiques, UMR 7358, 54000 Nancy, France.
f. Institut des Sciences de la Terre de Paris, UMR 7193, Sorbonne Université, CNRS-INSU, 75252 Paris, France.
g. Laboratoire d'Océanographie et du Climat: Expérimentations et Approches Numériques, UMR 7159 CNRS, IRD, Sorbonne Université/MNHN/IPSL, 75252 Paris, France.
* Corresponding author, e-mail address: ana.alves@mnhn.fr

Abstract

To date, little is known about the impact of super-eruptions on ocean biogeochemistry. Using boron isotopes ratios measured on planktonic foraminifera in the marine sediment core BAR94-25, we provide a high-resolution pH record in the Andaman Sea (North of Sumatra), spanning Marine Isotopic Stage 5 to 3. This transition encompasses the super-eruption of the Toba volcano, 74,000 years ago, making it possible to decipher the potential impact of the super-eruption emissions on the ocean pH for the first time. Our results show that inferred foraminiferal pH values generally follow those predicted by glacial-interglacial CO_2 variations. However, several abrupt pH drops coincide with Toba ash deposition. This suggests the occurrence of acidification events possibly related to Toba volcanic sulphur emission episodes. These pH drops are followed by anomalous pH increases, possibly relating to localised increases in seawater alkalinity following the alteration of large ash deposits on land.

Keywords

Toba

Volcanism

Ocean pH

Acidification

Paleoceanography

1 Introduction

Natural variations of atmospheric pCO_2 have a direct impact on ocean pH. During interglacial periods, the increase of atmospheric pCO_2 relative to glacial periods induces a surface ocean acidification due to the higher dissolution of CO_2 into the seawater (Hönisch and Hemming, 2005). During Pleistocene interglacial periods the average seawater pH was ~8.15 (Hönisch and Hemming, 2005). On the contrary, during glacial periods, the decrease of atmospheric pCO_2 increases surface ocean pH due to less dissolution of CO_2 into the seawater. The average seawater pH was ~8.3 with a glacial/interglacial pH amplitude of ~0.15 units (Hönisch and Hemming, 2005; Sanyal et al., 1995; Shao et al 2019). Throughout the transition from interglacial marine isotope stage (MIS) 5 to glacial MIS 4, a decrease of atmospheric pCO_2 is observed in the Vostok ice core (Petit et al., 1999) linked to an increase of surface ocean pH (Hönisch and Hemming, 2005). This corresponds to a period characterized by an increase of northern hemisphere ice caps and an associated drop in sea level (Rampino and Self, 1992; Waelbroeck et al., 2002).

While volcanism may also potentially impact surface ocean pH, to date few studies have assessed the impact of explosive super-eruptions on ocean pH. During the transition from MIS 5 to MIS 4, the largest explosive volcanic eruption of the Quaternary occurred, the Youngest Toba Tuff (YTT), with a volcanic explosivity index (VEI) >8 (Chesner, 2012; Ninkovich et al., 1978; Oppenheimer, 2002). The Toba volcano super-eruption is associated with the deposition over much of the North Indian Ocean of a thick ash layer known as the YTT (Fig. 1). The eruption occurred about 74,000 years ago in northern Sumatra (Fig. 1), Indonesia (Mark et al., 2017; Ninkovich et al., 1978; Oppenheimer, 2002; Rose and Chesner, 1990; Storey et al., 2012). In marine sediment cores, this ash layer is located during the increase of oxygen isotope ratios ($\delta^{18}O$) that marks the climatic transition between MIS 5 and MIS 4 (Ninkovich et al., 1978;

Schulz et al., 2002). The estimated volume of material emitted is of 5300 km^3 Dense Rock Equivalent (DRE) (Costa et al., 2014) resulting in the deposit of more than 5 mm of ash over 40 million km^2. Ash deposits have been found up to 9,000 km away from the eruptive center in South Africa on the African continent (Smith et al., 2018). Considerable uncertainties are associated with sulphur emissions, estimated for this eruption between 3.5 x 10^{10} kg and 3.3 x 10^{12} kg (Oppenheimer, 2002). The magnitude of the eruption and the amount of emissions leads to the hypothesis that it may have impacted the chemistry of the ocean surface. A recent study made on marine core BAR94-25 revealed multiple phases of Toba's last volcanic activity (Caron et al., 2023). Three main successive volcanic activity phases (VAP1 to VAP3) over a period of ~50 ka have been identified. The VAP2, which includes the YTT, is likely composed of 6 eruptive events over a period of ~10 ka. Repeated volcanic eruptions, imply a more prolonged and persistent impact on the ocean-atmosphere dynamics and climate.

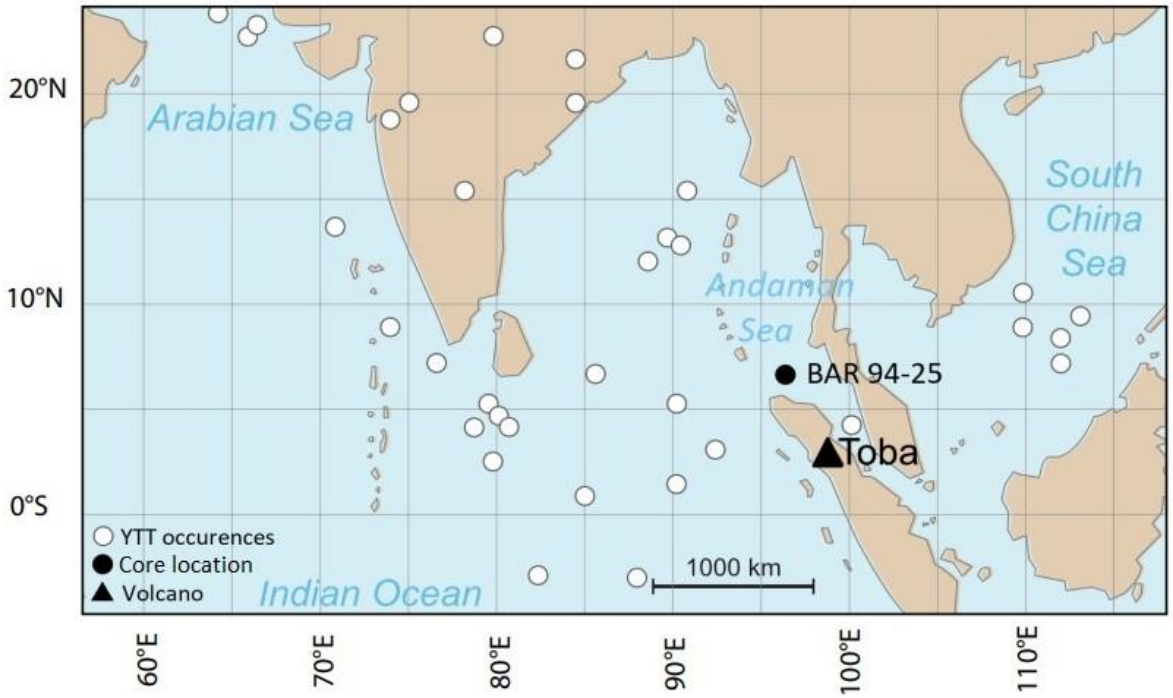

Fig. 1. Map with location of Toba volcano and study core. Location of Toba volcano (black triangle) and occurrences of the Youngest Toba Tuff (white dots) in the Indian Ocean, South

Asia and the South China Sea (modified after Lane et al., 2013). The black dot marks the location of core BAR94-25 (95°19.5'E; 6°26.09'N), North of Sumatra.

Large explosive volcanic eruptions can have multiple impacts on the Earth's climate and environments. These impacts are related to the emissions into the troposphere and stratosphere of ashes and different gas species, of which, sulphur emissions have the main climatic impact (Robock, 2000). Sulphur dioxide (SO_2) injection into the stratosphere leads to the formation of fine sulphuric acid droplets (H_2SO_4 aerosols). This can result in an increase of atmospheric opacity and a decrease of Earth's surface temperature, associated with changes in atmospheric circulation (Robock, 2000). Sulphur aerosols deposited on the ocean surface, through acid rain and ashfalls, can modify its chemistry (Langmann, 2014). Once in contact with seawater, sulphuric acid dissociates into sulfate ions (SO_4^{2-}) and hydrogen ions (H^+), which increase the sulfate concentration of the seawater, and decrease its pH (Doney et al., 2007). However, the effects impact of sulphuric acid on the acidification of seawater following explosive eruptions are still poorly explored.

In addition to flash acidification events the increase in alkalinity due to the weathering of volcanic material may affect seawater chemistry over longer timescales. Indeed, the atmospheric CO_2 consumption during chemical weathering of silicate rocks, and among them more efficiently volcanic rocks and pyroclastic material, is considered as a major process for balancing the global carbon cycle over geological timescales (Dessert et al., 2003; Gaillardet et al., 1999; Louvat and Allègre, 1997). The resulting riverine flux of bicarbonate and cations (e.g. Ca^{2+}, Mg^{2+}, Na^+, K^+) leads to an increase of ocean alkalinity. While the chemical alteration of basalts has been particularly highlighted as a feedback mechanism for major CO_2 emissions from large magmatic provinces (traps) over time scales ranging from tens to hundreds of

thousand years (e.g. Dessert et al., 2003; Jouini et al., 2023), the potential effects on alkalinity has received little attention in the case of super-eruptions. In the case of freshly erupted volcanic material (especially tephra), which is more easily and rapidly weathered than volcanic rocks, CO_2 consumption and seawater alkalinization could be much more rapid, on a millennial timescale or less (Börker et al., 2019; Jones et al., 2011).

The two aims of this work are (1) to reconstruct changes in ocean surface pH during the interglacial-glacial climate transitions MIS 5-MIS 4 and MIS 4-MIS 3 and (2) to assess the potential impact of the Toba's large volcanic emissions on ocean chemistry. To do so, we reconstructed, surface ocean pH variations at unprecedented high-resolution by measuring boron isotopes ($\delta^{11}B$) on pristine planktic foraminifera from marine core BAR94-25 located in the North of Sumatra, about 600 km from the Toba (van der Kaars et al., 2012) (Fig. 1). Close to the Toba eruptive center, this core provides a well-preserved sequence of tephra and cryptotephra, all belonging to the super-volcano (Caron et al., 2023), which makes it possible to unambiguously identify pH changes that could be associated with the multiple eruptions of Toba.

2 Materials and methods

2.1 Marine sediment core BAR94-25

Marine sediment core BAR94-25 was collected at a water depth of 1158 m in the Andaman Sea (6°26.09'N - 95°19.5'E), about 100 km North of Sumatra Island (Fig. 1), during the BARAT oceanographic cruise of Indonesian R/V Baruna Jaya in 1994. The total length of marine piston core BAR94-25 is 820 cm.

The present study concerns the 255-355 cm interval (Fig. S1 and S2) corresponding to the interglacial-glacial transition between the MIS 5 and MIS 4 and the main eruptions associated

with the Toba, including the YTT (Caron et al. 2023). Sediment core BAR94-25 was sampled approximately every 2 cm over the interval 258-353 cm for trace elements and stable isotopes analyses. Monospecific samples of the shallow dwelling planktic foraminifera *Globigerinoides ruber* senso stricto were used for the analyses (Fig. S3). Only well-preserved shells with no visual signs of alteration under binocular were picked. For boron isotopes and trace elements measurements, 100 shells from the 250-315 µm size fraction were used. Depending on availability, we picked 9 to 18 shells from the 250-315 µm fraction for oxygen and carbon isotope ratios analysis.

2.1.1 $\delta^{18}O$ planktonic foraminiferal analyses

New $\delta^{18}O$ data were obtained for this work and added to previously published data (Caron et al., 2023; van der Kaars et al., 2012), doubling the number of data points over the studied interval. Samples were analyzed at the *Laboratoire des Sciences du Climat et de l'Environnement* (LSCE) with a VG-Optima and a Finnigan IsoPrime mass-spectrometers. For the new data, replicate analyses were performed for each sample (twice 9 foraminifera) in order to decipher potential sample inhomogeneity and decrease the uncertainty. All results are expressed as $\delta^{18}O$ in per thousand (‰) relative to Vienna PeeDee Belemnite (V-PDB) standard. Analytical precision is calibrated with the international standards NBS 18 and NBS 19 (Carrara marble UCD-SM92). Internal analytical reproducibility is ± 0.05‰ 2SD. The details of the new age model are presented in the supplementary materials (Section 1, Fig. S4, S5 and Table S1)

2.1.2 Foraminiferal cleaning

We measured $\delta^{11}B$ on 53 samples of 100 *Globigerinoides ruber* ss. Foraminifera were washed following previously established protocol (Barker et al., 2003; Rae et al., 2011). The cleaning for $\delta^{11}B$ involves removing clays, organic matter and others non-dissolved contaminants. To

facilitate washing, it is necessary to gently crack the foraminifera between two glass slides under a binocular. The fragments were then transferred to a 500 µL Eppendorf tube with MQ water. To remove the clays, the samples are rinsed and ultrasonicated about 5 times with MQ water, until no clay residue is visible. An oxidative phase is then carried out to remove organic matter with 0.1 N NH_4OH buffered-1% H_2O_2 in a hot water bath at 80°C. The samples are then rinsed three times with MQ water and transferred to 1.5 mL Eppendorf tubes for leaching with 0.0005 N HNO_3 (pH ~3.3) to remove any adsorbed contaminants. They are then rinsed again with MQ water to eliminate 0.0005 N HNO_3 residuals. After cleaning, the samples were dissolved with 0.5 N HNO_3, for a final volume of around 100-200 µL. The samples were centrifuged 5 min immediately after dissolution and transferred to a Teflon vial for storage, leaving a residual volume of ~ 10 µL in the Eppendorf tube to exclude any remaining undissolved contaminant. Trace elements and $\delta^{11}B$ analysis are then both performed on this sample solution.

2.1.3 Foraminiferal trace element analysis

Trace elements were measured at *Institut de Physique du Globe de Paris* (IPGP) with a 7900 Agilent ICP-QMS (Inductively Coupled Plasma Quadrupole Mass Spectrometry). All samples were analyzed with the same calcium concentration in order to limit matrix effects (Yu et al., 2005). To check the efficacity of the cleaning protocol and determine the paleo-temperature of each sample, we respectively looked at the Al/Ca, Mn/Ca (indicator of clay and manganese oxide contaminations) and Mg/Ca ratios. The concentrations of Mg, Al, Ca and Mn were determined with a calibration curve by measuring two elementary calibrated solutions, one for trace and minor elements and one for major and minor elements.

To check the quality of Mg/Ca measurements, two carbonate reference materials (JCt-1 and MVS-1) and a reference solution mimicking a foraminifera sample solution (NIST RM 8301 Foram) were measured throughout the analytical sessions at the same calcium concentration (10 and 20 ppm) as the foraminifera samples. The giant clam JCt-1 (Hathorne et al., 2013) makes it possible to address the long-term reproducibility of the measurement. It gave a repeatability of 1.34 ± 0.02 mmol/mol (2SD, n=30), in good agreement with the literature (1.289 ± 0.045 mmol/mol (Hathorne et al., 2013) or 1.32 ± 0.02 mmol/mol (Raitzsch et al., 2018)). The second reference material, a brachiopod (*Magellania venosa*) MVS-1 (Jurikova et al., 2019), is used to correct the samples for instrumental drift, and exhibited a repeatability of 5.25 ± 0.06 mmol/mol close to the published value (Jurikova et al., 2019) of 5.11 ± 0.02 mmol/mol (2SD, n=21). The newly released reference carbonate solution NIST RM 8301 Foram was added to the measurement session and showed a repeatability of 2.68 ± 0.02 mmol/mol (2SD, n=21), in good agreement with the reference value of 2.62 ± 0.14 mmol/mol (Stewart et al., 2021). Taking into account these different certified reference material analyses, an average repeatability of 2 % is considered for the Mg/Ca measurements of the foraminifera samples.

2.1.4 Foraminifera boron isotopes analysis

To determine the boron isotopic ratio in foraminifera samples, we followed the analytical protocol developed by Buisson *et al.* (2021) at *Institut de Physique du Globe de Paris* (IPGP). To extract the boron, we used the microsublimation technique (Buisson et al., 2021; Gaillardet et al., 2001; Misra et al., 2014; Raitzsch et al., 2018), which involves a distillation process that takes advantage of the volatile nature of boron in the $B(OH)_3$ form, the only boron species present at acidic pH, to separate it from the rest of the matrix. For this, a 50 µL drop of the dissolved sample was loaded onto a cap of a pre-cleaned 5 mL Savillex Teflon legged conical

vial. The vial was then coated in an aluminum foil entirely except for the upper tip, and placed (still upside down) on a hotplate for 24 hours at 95°C. Vials are then removed from the hot plate, flipped downside up and allowed to cool for 15 min. The distillates we obtained were diluted with 450 µL of MQ water to reach a 0.05 normality of HNO_3 (Buisson et al., 2021; Louvat et al., 2019, 2014, 2011). The 0.5 mL solution is finally transferred to a 5 mL propylene tube and analyzed immediately (within the day).

Boron isotopes abundance ratios ($^{11}B/^{10}B$) were measured at low mass resolution with a MC-ICP-MS (Multiple Collector Inductively Coupled Plasma Mass Spectrometry) Neptune (ThermoFischer Scientific) at IPGP. Intensities were measured using respectively the L3 and H3 Faraday cups, equipped with 10^{13} Ω amplifiers dedicated to low signals. A µ-dDIHEN (demountable Direct Injection High-Efficiency Nebulization) direct injection system (Buisson et al., 2021; Louvat et al., 2019) was used to reduce washing times between injections, inject 100% of the sample into the plasma and thus increase the signal sensitivity. It couples a d-DIHEN (a long quartz nebulizer plugged directly in the torch instead of an injector) with a 6-port FAST valve and a gas displacement pump (GDP), allowing very low sample uptake rates and small sample volumes. The 50 µL sample loop of the FAST valve is filled with the solution, standard or reference material to be analyzed and then pushed to the nebulizer with a 0.05 HNO_3 carrier solution from the GDP fed by an argon flux at micro-flow rate. We fixed the mass flow meter of the GDP at 45-50 $\mu L.min^{-1}$ to obtain sample uptake rate of 25-30 $\mu L.min^{-1}$ and achieve a stable signal plateau lasting ~ 100 s for the injections peaks, which allows to measure the $^{11}B/^{10}B$ ratio with 12 cycles of 8 seconds (Buisson et al., 2021; Louvat et al., 2019). Prior to the boron isotopes analysis, boron concentrations were roughly measured on the MC-ICP-MS in order to match within ± 5% the concentrations of the sample, standard and reference material

239 solutions. NIST SRM 951 standard (Catanzaro, 1970) was used as bracketing standard to get
240 rid of the instrumental mass bias.
241
242 Each sample was measured three times according within the following sequence: Blk – Std –
243 Sample – Std – Sample – Std – Sample – Std – Blk. Average blank signals were subtracted
244 from the sample and standard signals. The $\delta^{11}B$ of each replicate was calculated as the relative
245 deviation of $^{11}B/^{10}B$ ratio of the sample to that of the standard, and expressed in ‰. Five values
246 of $\delta^{11}B$ can be calculated from the triplicate sample-standard bracketing of one sample (Buisson
247 et al., 2021; Louvat et al., 2019). Sample average $\delta^{11}B$ and repeatability (2SD) are then
248 calculated. *Globigerinoides ruber* foraminifera species exhibit high boron concentrations: thus,
249 with 100 individuals of the 250-315 µm size fraction, [B] after microsublimation were between
250 4.5 and 15 ppb. To verify the quality of the purifications (yield close to 100 %), we added the
251 reference carbonate material MVS-1 (Jurikova et al., 2019) and the reference carbonate solution
252 NIST RM 8301 Foram (Stewart et al., 2021) to the microsublimation sessions, for charged B
253 masses of 2.5 and 5 ng (final [B] of 5 and 10 ppb) in the range of those for foraminifera samples.
254 Measurements of MVS-1 yielded an average value of 15.87 ± 0.28 ‰ (2SD, n=10) in agreement
255 with its reference value (15.95 ± 0.19‰, n=46, Jurikova et al., 2019), and NIST RM 8301
256 Foram analyses exhibited an average value of 14.49 ± 0.21 ‰ (2SD, n=10), also in full
257 agreement with its reference value (14.51 ± 0.17 ‰, Stewart et al., 2021). Blanks were also
258 measured to monitor boron contamination during the whole procedure. Blank boron amounts
259 were all lower than 17.5 pg (8 ± 8 pg, n=15, 1SD), representing therefore only 0.2% of the
260 amount of boron of the least concentrated sample. Finally, the AE121 reference material
261 solution (Vogl and Rosner, 2012) was regularly measured during the analytical sessions, with
262 an average $\delta^{11}B$ value of 19.60 ± 0.27‰ (2SD, n=35) for [B] between 4.5 and 15 ppb, in
263 agreement with the reference value 19.9 ± 0.6‰ and more specifically within the IPGP long-

term reproducibility of 19.56 ± 0.17‰ (2SD, n=90, for [B] of 100-200 ppb (Louvat et al., 2019)) and 19.60 ± 0.23‰ (2SD, n=43, for [B] of 4-10 ppb (Buisson et al., 2021)).

2.2 Seawater pH

In order to reconstruct pH from foraminiferal boron isotopes, species-specific calibrations are first used to transform $\delta^{11}B_{calcite}$ into $\delta^{11}B_{borate}$. Such calibrations allow us to correct the species dependent vital effect inherent to planktic foraminifera (Henehan et al., 2016, 2013).

We applied the calibration of De La Vega *et al.* (2023), for *Globigerinoides ruber*, which uses the glacial-interglacial CO_2 record to optimize the calibration of Henehan *et al.* (2013).

$$\delta^{11}B_{borate} = (\delta^{11}B_{calcite} - 6.46)/0.72$$

Using either the calibration of Henehan *et al.* (2013) or Guillermic *et al.* (2020), makes no difference on the global observed trends but increases the magnitude of the observed anomalies (Fig. S6). For each sample, we computed the uncertainty on $\delta^{11}B_{borate}$ by quadratically propagating the analytical uncertainty associated with each $\delta^{11}B_{calcite}$ measurement (typically ±0.25‰ 2SD) and ±0.25‰ standard error associated with the calibration (Henehan et al., 2013).

To calculate pH, we used the following equation that considers seawater $\delta^{11}B$:

$$pH = pK^*_B - \log\left(-\left(\delta^{11}B_{sw} - \delta^{11}B_{borate}\right) / \left(\delta^{11}B_{sw} - \alpha * \delta^{11}B_{borate} - \varepsilon\right)\right)$$

where pK^*_B is the dissociation constant for boric acid at in situ temperature, salinity and pressure. $\delta^{11}B_{sw}$ is the isotopic composition of seawater. α is the experimentally determined equilibrium fractionation constant of 1.0272 ± 0.0006 (Klochko et al., 2006), and ε is 1000 x α. For our study, we used the MgCaRB software package developed by Gray & Evans (2019)

which requires past $\delta^{11}B$ seawater composition, pressure, salinity and temperature determined by iteratively solving with Mg/Ca (Gray et al., 2018) (Fig. S7). Due to its long residence time of 10 to 20 Myr longer than the ocean mixing time (Lemarchand et al., 2002), boron isotopic ratio in seawater therefore remains invariant over the period and time interval studied here. The modern seawater $\delta^{11}B$ value of 39.61 ± 0.20 ‰ is then set up for the whole interval of this study (Foster et al., 2010). In the same way, the pressure is fixed at 0 bar for all paleo-pH determinations, *G. ruber* living between 0 and 50 cm depth (Schiebel et al., 2018). Finally, the salinity is initialized in the MgCaRB tool at 32 psu, the present-day salinity of Andaman Sea (Sarma and Narvekar, 2001). For the studied range of this study, the salinity is then estimated according to sea level curve of Spratt and Lisiecki (2016) with an uncertainty of ± 1 PSU (2σ) (Gray and Evans, 2019; Lisiecki and Stern, 2016).

The main asset of the MgCaRB tool is to take into account the effects of salinity and carbonate chemistry on the Mg/Ca paleothermometer proxy for different foraminifera species-specific calibrations (Gray et al., 2018; Gray and Evans, 2019). Whereas the salinity has a limited impact on the reconstructed temperatures (SST), the implication of the carbonate chemistry through the pH or pCO_2 needs to be considered (Gray and Evans, 2019). The calculated $\delta^{11}B_{borate}$ of each sample and its associated 2SD value integrated in the MgCaRB software allowed to solve iteratively the Mg/Ca-temperature relationship for the *G. ruber* calibration:

$$\text{Mg/Ca (mmol/mol)} = \exp(0.036(S-35) + 0.064T - 0.87(pH-8) - 0.03),$$

where S is salinity (PSU) and T is temperature in °C. Then the final pH is calculated for each sample, with Monte-Carlo propagation to determine the final uncertainties. Finally, to reveal trends in the timeseries we fit the resulting pH estimates with a LOESS regression, propagating

the uncertainties via Monte-Carlo simulation. In order to determine pH changes driven by processes beyond changing atmospheric CO_2, we estimate the equilibrium pH using the atmospheric pCO_2 record (Bereiter et al., 2015), an estimate of alkalinity, which we take as a flat probability distribution between the modern alkalinity minus 25 µmol/kg and modern alkalinity plus 50 µmol/kg, broadly encompassing the expected whole-ocean change over a glacial cycle (Gray and Evans, 2019; Martínez-Botí et al., 2015; Toggweiler, 1999), and SST and SSS estimates in the manner described above. As a sensitivity test, we also estimate equilibrium pH assuming an alkalinity addition of 250 µmol/kg.

2.3 Planktic foraminiferal calcification intensity

The weight/size ratio of the foraminifera is used as a proxy for calcification intensity (Weinkauf et al. 2013). As the same size range (250-315 µm) was used for all samples, only weight was measured. Prior to weighing, the shells were ultrasonically cleaned in a methanol (CH_3OH) bath to remove clays and other contaminants. The mean weight of planktic foraminifera was obtained by weighing between 9 and 18 shells of *Globigerinoides ruber* from the 250-315 µm size fraction using a Mettler Toledo XP2U microbalance with an accuracy of 0.1 µg at LSCE. The weight was then divided by the number of shells. Most samples consisted of 18 shells that were divided into two groups of 9 shells and weighed. This allowed to estimate the standard deviation (1σ) between the two values obtained for the two groups of 9 shells of the same range of size.

2.4 Published data

Other data already published (Caron et al., 2023; van der Kaars et al., 2012) were used in our work: K/Ti and Ca high resolution records (0.5 cm) derived from X-ray fluorescence (XRF) and, tephra counting estimated from the decarbonated fraction >63µm at cm-scale. The XRF-

Ca fraction was used to construct a high resolution $CaCO_3$ record (Fig. S8) while the K/Ti ratio was used to identify ash deposits, as they are enriched in potassium (K) in relation with hemipelagic sediments (Westerhold et al., 2009).

3 Results

Core BAR94-25 was studied from 255 to 355 cm depth, which corresponds to the time interval from MIS 3 to MIS 5 (~ 54 to 87 ka) based on planktic foraminifera *Globigerinoides ruber* white $\delta^{18}O$ stratigraphy (Fig. 2a, see Supplementary Materials, section 1 Age Model).

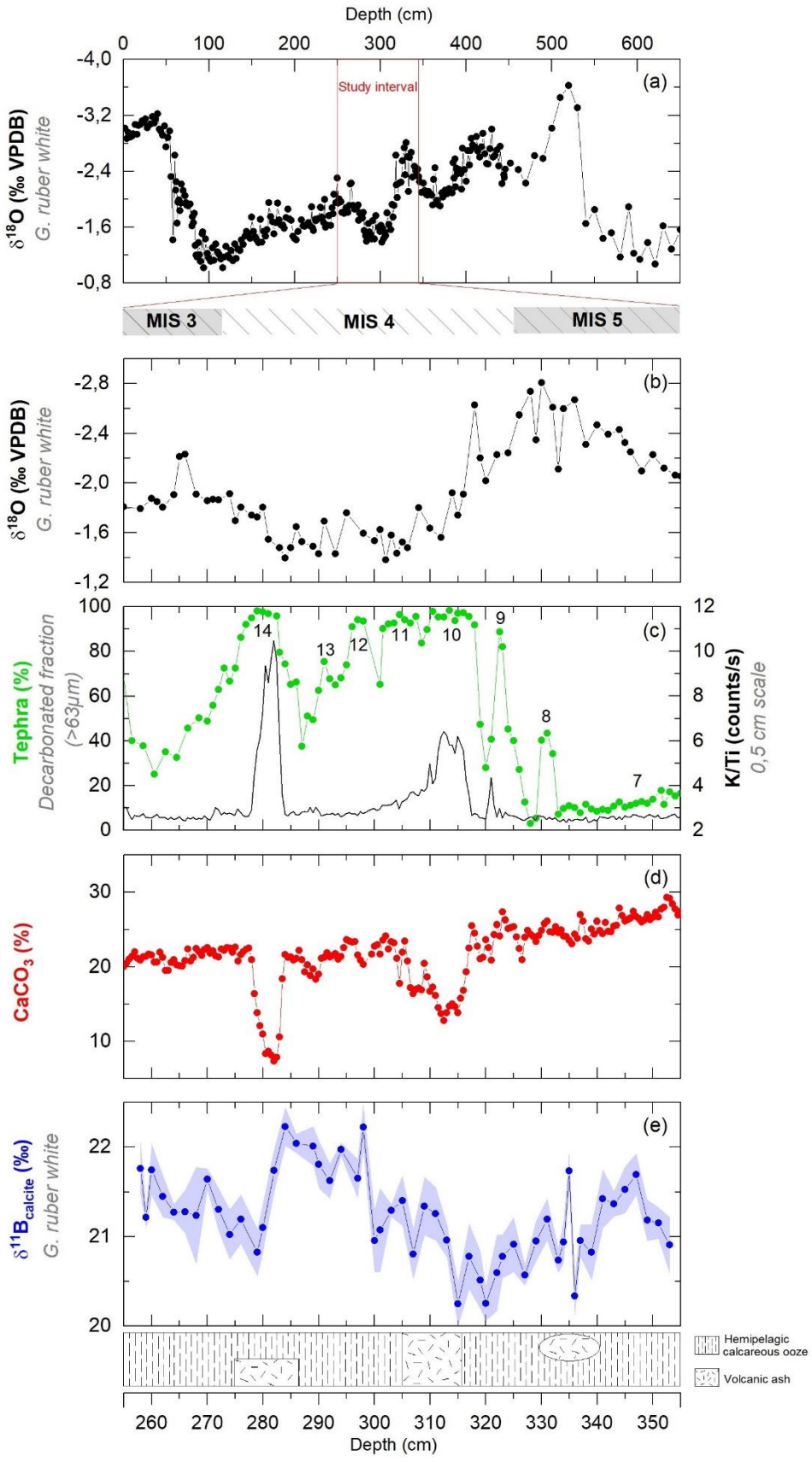

Fig. 2. Data from core BA94-25. (a, b), $\delta^{18}O$ from planktic foraminifera *Globigerinoides ruber* (250-315 µm size fraction). (c), Percentage of tephra in the decarbonated sediment fraction >

63 µm (green line) and K/Ti ratio (black line) determined by bulk sediment XRF. (d), $CaCO_3$ content of the sediment core. (e), $\delta^{11}B$ from planktic foraminifera *Globigerinoides ruber* (250-315 µm size fraction) and 2SD uncertainties. The lithological log of the core, shows visible layers of tephra within the main hemipelagic calcareous ooze lithology.

A previous study combining the counting of tephra percentages in the decarbonated fraction (>63µm) and trace element analyses of ashes, enable the identification of seven tephra and cryptotephra layers in this interval classed in two Toba eruptive phases (called thereafter Volcanic Activity Phases, VAP) (Caron et al., 2023) with those numbered 8 to 13 belonging to VAP2 and the one numbered 14 to VAP3 (Fig. 2c). Ash layers 9 (from 320 to 326 cm), 10 (from 309 to 318 cm) and 14 (from 275 to 284 cm) corresponded to increasing of K/Ti ratio (Fig. 2c**)**. In particular, the layers 10 and 14, characterized by 98% of tephra showed the largest increases in the K/Ti ratio, while the layer 9 showed a slight increase in the K/Ti ratio consistent with 40% of tephra.

The $CaCO_3$ content of the total sediment ranges from 7 to 30% with an average of 25% (Fig. 2d). There are no significant glacial/interglacial changes, but the records show two marked drops in $CaCO_3$ values (< 20%) between 311.5 and 318.5 cm during MIS 4, and between 279.5 and 284.5 cm depth during MIS 3. The first of these drops has a complex structure. After reaching the minimum value, the $CaCO_3$ record shows a two-step increase towards higher values. The shallower interval of low $CaCO_3$ content has a simpler structure, with a sharp drop in $CaCO_3$ content followed by a rapid increase. These two low $CaCO_3$ intervals correspond to the two visible naked eye tephra layers (10 and 14). They are also correlated with a high K/Ti ratio (Fig. 2c**)**. Combined, the $CaCO_3$ content and K/Ti ratio of the total sediment, identify Toba ashfall events (10 and 14) of greater amplitude at this site in the Andaman Sea, which likely

diluted the background hemipelagic sediments. In particular, the large ashfall event 10 within the MIS 5-MIS 4 transition corresponds to the YTT layer widely reported in the Indian Ocean.

3.1 $\delta^{11}B$ record

The $\delta^{11}B$ values of planktic foraminifera *G. ruber* (Fig. 2e) range from 20.25 ± 0.19 to 22.22 ± 0.26 ‰ with an average of 21.23 ± 0.25 ‰ (2SD, n=53). To the first order, $\delta^{11}B$ values appear to follow oxygen isotope values, showing that boron isotope values follow glacial/interglacial variations (Fig. 2). This is with the exception of the interval from 330 cm to 315 cm in the lower part of the MIS 5-MIS 4 transition, where opposite trends with increasing $\delta^{18}O$ values and decreasing $\delta^{11}B$ values to the minima are perceptible. The minimum values of $\delta^{11}B$ at 320 and 315 cm correspond to volcanic events 9 and 10. Event 9 is characterized by a small decrease in $CaCO_3$ and event 10 by a much larger decrease in $CaCO_3$. Then the $\delta^{11}B$ increases again and shows a much higher range of values, with an abrupt increase of ~ 1‰ from 300 cm to 284 cm. This upward trend is interspersed with a large amplitude decrease at ~ 284 cm, with $\delta^{11}B$ values dropping from 22.23 ± 0.22 to 20.82 ± 0.27‰ within an interval of five centimeters, consistent with volcanic event 14 and a significant decrease in $CaCO_3$. As the $\delta^{18}O$ stratigraphy shows, this interval extends from the maximum of MIS 4 to the MIS 4-MIS 3 transition.

3.2 Weight of *Globigerinoides ruber* test

In the Andaman Sea, the average weight of a *Globigerinoides ruber* test with a range size of 250-315 µm is ~ 13 µg from 0 to 107 ka. At first order, *G. ruber* weight variations appear to follow the glacial-interglacial variations of the oxygen curve, with lighter values during interglacial periods and heavier values during glacial periods (Fig. 3). However, during MIS 4, two decreases in *G. ruber* weight (at 70 and 62 ka) coincide with Toba eruptive events 10 and 14, as well as strong decreases in $CaCO_3$ sediment content and *G. ruber* $\delta^{11}B$ values (Fig. 2).

The decrease of the weight of *G. ruber* observed during eruptive event 10 reaches the minimum value of the entire record. While, the decrease of the weight of *G. ruber* associated with eruptive event 14 is not significant enough to be distinguished from the background variability (Fig. 3). It is also noteworthy that a strong decrease in both *G. ruber* weight and $CaCO_3$ sediment content coincides with the Toba explosive event 6, not studied here (Fig.3).

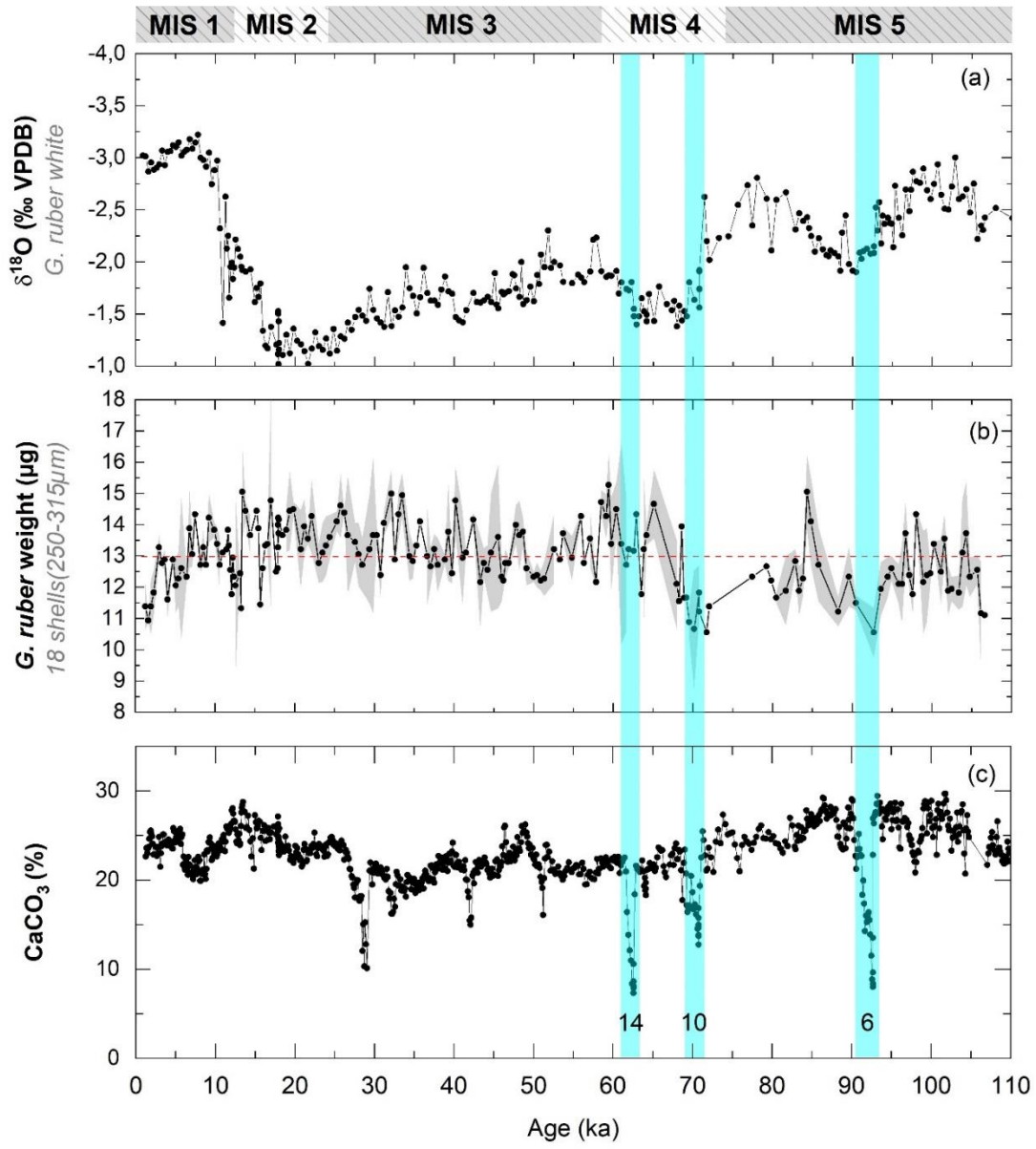

Fig. 3. Variations of *G. ruber* weight. (a), High resolution stable oxygen isotope ($\delta^{18}O$) record from core BAR94-25 measured in *G. ruber*. This record includes the previous data published (Caron et al., 2023; van der Kaars et al., 2012), and new data obtained for this study. (b)**,** *G. ruber* mean weight calculated with 9 to 18 shells from fraction 250-315µm and1σ uncertainty (gray). The red line represents the mean value for the whole record. The blue bars represent three visible tephra layers (6, 10 and 14), corresponding to Toba explosive eruptive phases VAP1, VAP2 and VAP3 (Caron et al., 2023). The tephra layer 10 is here interpreted as the paroxysmal YTT event. (c)**,** $CaCO_3$ content of the sediment core.

4 Discussion

4.1 Primary environmental signature of the boron isotope ratios

Before using foraminiferal boron isotopes to reconstruct seawater pH (see Methods 2.2 section), we assess the robustness of the obtained $\delta^{11}B$ data as a record of the primary environmental signal. Therefore, we first evaluated if they were unaffected by contamination from non-carbonate fractions or diagenetic processes. We used the Al/Ca and Mn/Ca ratios, measured on the same samples from which the $\delta^{11}B$ analyses were performed, as tracers of clay and oxide coating contamination, respectively (Rae et al. 2011; Gutjahr et al., 2017; Martin and Lea, 2002; Raitzsch et al., 2018). The fact that no correlation between Al/Ca or Mn/Ca and $\delta^{11}B$ values has been found for the entire dataset (Fig. S9) allows us to rule out the influence of contaminants on the boron isotopic composition (for more details see chapter 2 in Supplementary Materials). In addition, the tests of *Globigerinoides ruber* from the analyzed samples are very well preserved. The specimens, carefully examined by SEM images, show a pristine, unaltered surface texture with no signs of dissolution or authigenic overgrowth crystals (Fig. S3), ruling out a significant influence of taphonomic or diagenesis processes on boron isotope ratios.

In summary, the boron isotope ratios of the analyzed samples of *Globigerinoides ruber* trace the surface seawater pH and seem not affected by contamination, or diagenetic and taphonomic processes.

4.2 Surface seawater pH during the climatic transitions MIS 5-MIS 4 and MIS 4-MIS 3

Previous works show a strong linear relationship between glacial-interglacial atmospheric CO_2 variations recorded in ice-cores (Fig. 4a) and surface ocean pH derived from planktic foraminiferal boron isotopes (De La Vega et al., 2023; Hönisch and Hemming, 2005; Shao et al 2019). To test whether the Andaman Sea surface pH record derived from surface-dwelling *G. ruber* $\delta^{11}B$ is also mainly controlled by glacial-interglacial atmospheric CO_2 variations, we

compare it with the pH predicted by atmospheric CO_2 variations recorded in ice cores during the interval from MIS5 to MIS3, using the MgCaRB software package developed by Gray & Evans (Gray and Evans, 2019) (see Methods 2.4 section). The Figure 4b compares surface pH variations in the Andaman Sea (black dots and line), reconstructed from boron isotopes of *G. ruber,* with those reconstructed from ice core pCO_2 data (green line), assuming an equilibrium of surface water with atmospheric CO_2 variations. Sea surface pH reconstructed from atmospheric pCO_2 in ice cores (Fig. 4b, green line) covaries with interglacial-glacial variations of atmospheric CO_2 recorded in ice cores (Fig. 4a). During the last part of the warm interglacial MIS 5 covered by our high-resolution record, pH derived from pCO_2 shows low values with a clear minimum associated with the lowest $\delta^{18}O$ values (i.e. MIS 5.1). After this climatic optimum, the interglacial-glacial transition (i.e. increase of the $\delta^{18}O$ values from 78 to 70 ka), the global reduction in atmospheric pCO_2 (De La Vega et al., 2023; Foster, 2008; Sanyal et al., 1995) translates into an increase of pCO_2-derived sea surface pH from 8.19 to 8.22. During the glacial MIS 4, characterized by the highest $\delta^{18}O$ values, sea surface pH derived from pCO_2 increases continuously to reach a maximum value of 8.27 (i.e. minimum value of atmospheric CO_2) (Hönisch and Hemming, 2005; Sanyal et al., 1995). During the glacial-interglacial transition from MIS 4 to MIS 3, the evolution of atmospheric CO_2 leads to a decrease of the pCO_2-derived pH, which extends in MIS 3 until the pH reaches 8.22.

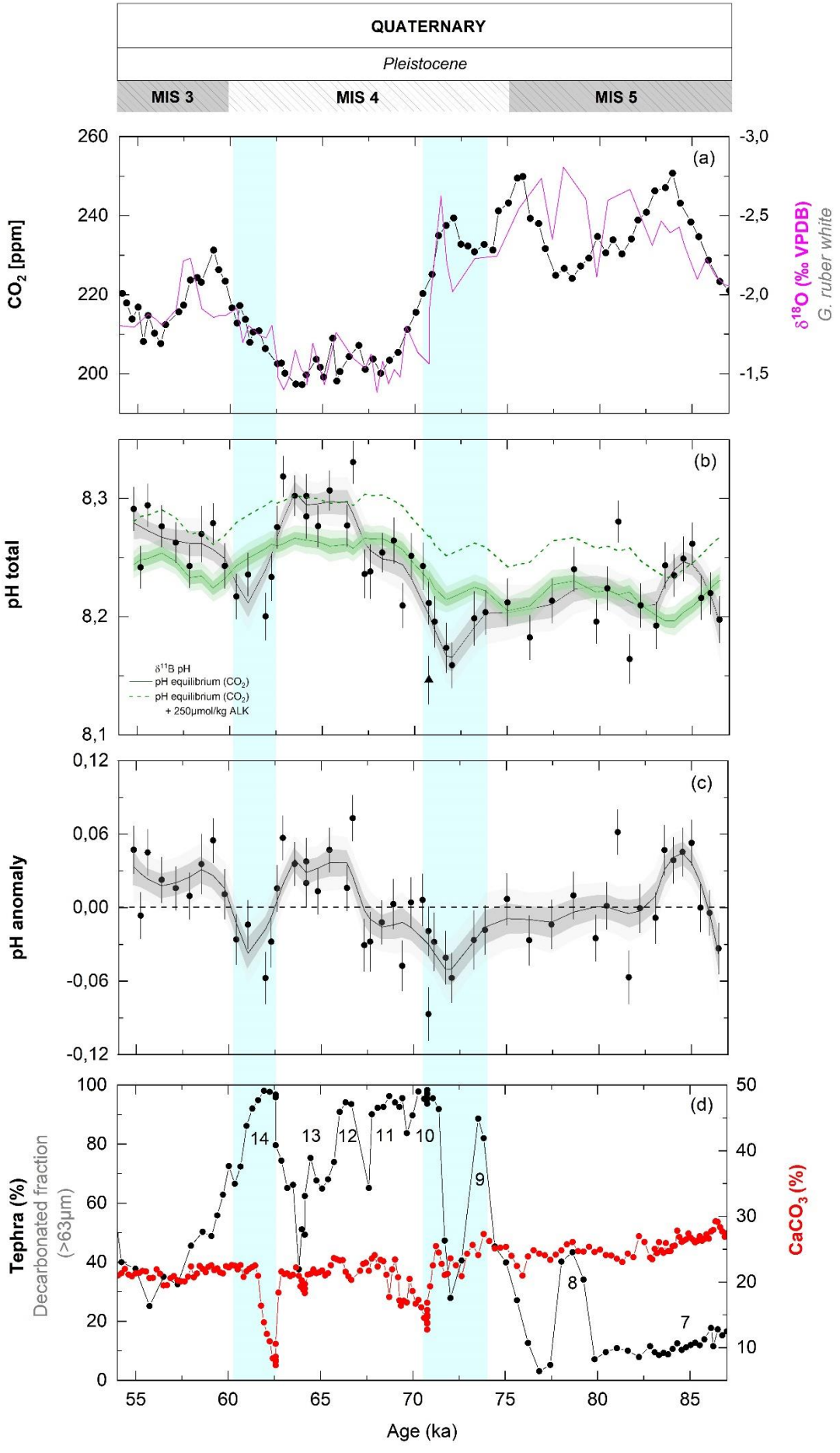
QUATERNARY
Pleistocene
MIS 3
MIS 4
MIS 5
(a)
CO2 [ppm]
δ18O (‰ VPDB)
G. ruber white
(b)
pH total
δ11B pH
pH equilibrium (CO2)
pH equilibrium (CO2)
+ 250µmol/kg ALK
(c)
pH anomaly
(d)
Tephra (%)
Decarbonated fraction
(>63µm)
CaCO3 (%)
14
13
12
11
10
9
8
7
Age (ka)

463

Fig. 4. Data from core BA94-25. (a), Atmospheric CO_2 concentrations from Antarctica ice cores (black) (Bereiter et al., 2014) and $\delta^{18}O$ of planktic foraminifera *G. ruber* (pink) from Andaman Sea. (b), pH of surface of the Andaman Sea reconstructed from boron isotopes (black dots) and 2σ uncertainty, loess regression of pH data that shows the trends (black line) and 2σ uncertainty (gray), pH of surface of the Andaman Sea reconstructed from ice core pCO_2 data (green line) and 2σ uncertainty (light green), assuming an equilibrium of surface water with atmospheric CO_2 variations and adding 250µmol/kg to alkalinity (green dash line). (c), pH anomaly that corresponds to the difference between pH of the Andaman Sea derived from *G. ruber* boron isotopes and from atmospheric CO_2 ice-core record (black dots), loess regression of pH anomaly (black line) and 2σ uncertainty (gray). (d), Percentage of tephra in the decarbonated sediment fraction > 63 µm (black line) and $CaCO_3$ content of the sediment core (red line).

Changes in the *G. ruber* $\delta^{11}B$-derived pH in the Andaman Sea record (at a resolution step of ~ 500 years) largely reproduce pCO_2-derived pH variations, indicating that first-order $\delta^{11}B$-pH variations follow interglacial-glacial changes in atmospheric CO_2 (Fig. 4), similar to previous works (Hönisch and Hemming, 2005; Foster 2008; De La Vega et al., 2023; Shao et al 2019). However, closer observation reveals notable discrepancies. First, during the MIS 5-MIS 4 transition, our data show an unexpected decrease in pH from 8.24 to 8.14, whereas pCO_2-derived pH shows an increase (Fig. 4b**)**. Secondly, $\delta^{11}B$-derived pH indicates an abrupt decrease of 0.13 pH units during MIS 4-MIS 3 transition, while pCO_2-derived pH result in a much smaller and smoother change (~ 0.03 pH units). Finally, following both unexpected pH decreases, a period with a higher $\delta^{11}B$-derived pH is observed with average values of 8.3. These anomalously low and high pH values do not seem to be related to CO_2 variations, and in the following section we discuss if and how they are related to the eruptive activity of Toba.

4.3 Surface seawater pH perturbations associated with the Toba eruptive activity

Core BAR94-25 records the volcanic activity of Toba volcano and its impact on the Andaman Sea. On this same core, other studies conclude that the well-known YTT event was preceded and followed by other volcanic eruptions that could also be attributed to the Toba volcano on the basis of their geochemical signatures (Caron et al., 2023). Our own observations show the existence of two main explosive volcanic events (events 10 and 14) characterized by a high content of volcanic material that induces sharp drops in $CaCO_3$ content (Fig. 4d). According to their stratigraphic position, the eruptive event 10 could correspond to the YTT within the VAP2, while the eruptive event 14 could correspond to a post-YTT eruption within the VAP3.

During the interglacial MIS 5, $\delta^{11}B$-derived pH values in the Andaman Sea vary between 8.25 and 8.20. A drop in pH takes place during the eruptive activity, with values decreasing from 8.21 to 8.14 in coincidence with volcanic events 9 and 10. The pH drop begins during event 9, but the lowest pH value of 8.14 is observed during event 10. In this case, the effects of eruptive events 9 and 10 cannot be distinguished. Note that the pH curve has been smoothed (LOESS regression) to better distinguish the main anomalies from the background values. Eruptive events 9 and 10 were probably close together and their effects cannot be distinguished because the time resolution of the smoothed pH curve is much lower than that of the tephra curve. This pH reduction associated with the eruptive events 9 and 10, is followed by an increase of pH up to 8.33 at the end of the volcanic event 12. Between volcanic events 12 and 14, high values of pH can be observed between 8.27 and 8.33, higher than the pCO_2-derived pH (~ 8.26). Finally, in coincidence with volcanic event 14, a decrease in pH values from 8.31 to 8.21 is observed. This is the largest decrease observed during the whole period that also coincides with a sharp $CaCO_3$ drop.

Our results suggest that in the Andaman Sea the volcanic activity of Toba was associated with a significant decrease in both the sea surface pH and in $CaCO_3$ accumulation in sediments. In ocean sediments, such as the core studied here, the calcium carbonate content mainly or exclusively reflects the relative weight contribution of carbonate shells and remains of planktic organisms (i.e. planktic foraminifera, coccoliths). The significant dilution of hemipelagic sediments by ash during events 10 and 14 is partly responsible for these $CaCO_3$ decreases. The fact that they also coincide with a decrease in pH suggests that they could also have been induced by transient acidification events caused by the eruptions. An episode of ocean acidification is characterized by a decrease in pH and also by a decrease in calcium carbonate saturation state (Hönisch et al., 2012; Zeebe, 2012), that could result in a decrease in biocalcification and/or increase in dissolution, and consequently in its reduced accumulation in sediments. Although the response of marine calcifying organisms to ocean acidification is complex and not uniform according the different taxa and species, several studies confirm that planktic foraminiferal calcification intensity decreases under more acidic seawater conditions (Dong et al., 2022; Henehan et al., 2017). Decreases in the weight of *G. ruber* tests of the same size range, which is a proxy for calcification intensity, were observed in the core BAR94-25 in the tephra layers 10 (VAP2) and 14 (VAP3). These are both associated with decreases in bulk sediment $CaCO_3$ and pH. However, the calcification intensity of *G. ruber* shows a smaller decrease during eruptive event 14 than during eruptive event 10 (Fig. 3). This could be explained by the fact that in the coincidence of eruptive event 10 the lowest surface seawater pH values (8.14) of the whole interval studied were reached, whereas in the coincidence of eruptive event 14, although the pH drop was much more pronounced, the values remained higher (8.20) because the drop itself started from anomalously high values (8.32) (Fig. 4). As the preservation of the analyzed *G. ruber* tests is excellent (Fig. S3), the decrease in their weight is not due to post-mortem dissolution, but probably to a decrease in biocalcification intensity

when the foraminifera were alive (Dong et al., 2022; Henehan et al., 2017) related to the decrease in surface seawater pH and calcite saturation due to variations of seawater carbonate ion concentration (CO_3^{2-}). Part of the decrease in $CaCO_3$ during volcanic events, beyond the dilution effect of ash fall, could therefore be related to a decrease in the intensity of foraminiferal calcification due to the acidifying effect of the eruptions themselves.

These transient episodes of acidification do not appear to have been caused by episodes of increased atmospheric CO_2, as shown by their discrepancies with the CO_2-derived pH curve (Fig. 4). Rather, they could be the result of the largest sulphur emissions from Toba, which led to the deposition of acidic sulphur aerosols on the ocean surface via acid rain and ash (Langmann, 2014), thereby modifying the surface seawater pH of the Andaman Sea. A recent work shows that a significant proportion of the sulphur emitted during explosive eruptions (up to 40%) can be transported to the ocean surface by ash fallout in the form of aerosols absorbed on volcanic glass (Langmann, 2014). This mechanism might have facilitated the seawater acidification in areas where Toba ash fallout was most intense. Sulphur-induced acidification events may have reduced the production of calcium carbonate by calcareous plankton and, consequently, its accumulation in sediments.

On this basis, we estimated the sulphur input required to acidify the mixed layer (first 50 m) of the Andaman Sea by 0.1 pH unit (see Supplementary Material, section 3 for more details). The estimated amount of sulphur required for this acidification would be ~ 4.06×10^6 kg, which is substantially lower than estimates for the total sulfur emitted from the Toba super-eruption (3.5×10^{10} kg to 3.3×10^{12} kg, Oppenheimer et al., 2002). On the other hand, if we hypothesize that the entire surface of the global ocean was acidified by 0.1 pH units, the required sulphur input would be ~ 1.84×10^9 kg, a quantity approaching the lowest estimation of sulphur emissions

from the Toba supereruption in the literature (3.5 x 10^{10} kg, Oppenheimer et al., 2002). Thus, while the available estimates on magnitude of sulphur emitted from Toba of the magnitude required to acidify the ocean globally, we would need other similar high-resolution pH records from other sites, which do not currently exist, to verify whether the Toba volcanic activity had a local or global effect on the surface ocean. Overall, our results highlight the potential for super eruptions to impact ocean carbonate chemistry and biocalcification of planktic foraminifera. Finally, we note that due to the temporal averaging inherent to foraminiferal samples from sediment cores (which typically represent at least a century), the true magnitude of the pH decrease may have been larger, and the true duration of the event may have been shorter than observed.

Following the acidification associated with the major ash fall event 10, an increase in the pH of the Andaman Sea surface to anomalously high values, relative to the pCO_2-derived pH, is observed (Fig. 4). An anomalous pH increase is also present following the ash fall event 14, but on a smaller magnitude (Fig. 4). This pH increase is associated with the recovery of $CaCO_3$ accumulation in the sediments and reduced ashfall, as indicated by low K/Ti ratios in the bulk sediments (Fig. 2 and Fig. 4). We propose the pH increase may relate to a localised increase of alkalinity in the Andaman Sea, sourced from an enhanced chemical weathering of large ash deposits from the paroxysmal eruptive activity of Toba: the chemical weathering of these fresh tephra deposits, widely dispersed in the surrounding lands and seawater, would have increased atmospheric CO_2 consumption and the resulting flux of HCO_3^- and cations (Ca^{2+}, Mg^{2+}, Na^+, K^+) from rivers or groundwaters, leading to an increase in seawater alkalinity and pH (Börker et al., 2019; Jones et al., 2011). A large part of the CO_2 emitted by a volcano may also be consumed by such weathering process and increase ocean alkalinity (Dessert et al., 2003; Rivé et al., 2013). This process has been invoked in particular in the case of large magma provinces

(traps) on timescales of tens to hundreds of thousands of years (Dessert et al., 2003; Jouini et al., 2023). However, fresh volcanic rocks and ash weathers much faster (Börker et al., 2019). Volcanic ashes and ejecta might weather especially fast, because of a relatively high glass content (Wolff-Boenisch et al., 2006) and high reactive surface area. Thus, a time scale of a few millennia or less between the major ash-fall events (10 and 14) and the anomalous rises in pH should be compatible with alkalinization events due to the chemical weathering of a huge quantity of easily erodible ash and ejecta.

To test this hypothesis, we estimate that the observed anomalous increase in pH of ~0.05 following the volcanic event 10 should correspond to an alkalinity variation of 250 µmol/kgSW (Fig. 4b), requiring in an alkalinity flux of 9.97×10^{12} mol to the Andaman sea (see Supplementary Material, section 4 for more details). Based on studies of weathering rates in nearby Java, we estimated a first order alkalinity flux from the weathering and runoff of the YTT deposits on Sumatra (see Supplementary Material, section 4 for more details) between 1 and 10×10^6 mol/km^2/yr, resulting in an alkalinity flux of between 15×10^9 and 1.5×10^{11} mol/yr to the Andaman Sea. Considering the maximum value of alkalinity flux obtained (1.5×10^{11} mol/yr), it would take ~100 years to increase the pH of the surficial Andaman Sea by ~0.05. This is around 10 times longer than the residence time surface waters, hence alkalinity fluxes following the Toba eruption would need to be approximately ten times higher than the estimates considered above to account for the pH increase alone. Thus, while the available estimates of alkalinity flux cannot fully explain the observed pH increases, the uncertainties on these estimates are very large, and these estimates highlight the potential of large ash deposits as a source of alkalinity to drive changes in ocean pH.

Conclusions

This study presents for the first time a high-resolution record of surface seawater pH in the Andaman Sea, spanning MIS 5 to MIS 3. The sea surface pH reconstruction based on $\delta^{11}B$ measurements of the planktonic foraminifera *G. ruber* senso stricto from core BAR94-25, recorded a strong imprint of the different eruptions of the Toba volcano, during the study interval.

Comparison of the Andaman Sea pH record derived from *G. ruber* $\delta^{11}B$ with the pH predicted by atmospheric CO_2 variations recorded in ice cores, showed that at long-term, the surface seawater pH was largely controlled by glacial-interglacial atmospheric CO_2 variations, as shown by previous studies for other oceanic sites. However, it also revealed several anomalous pH values in the Andaman Sea associated with Toba's explosive activity, in particular eruption 10, which probably corresponds to the paroxysmal eruption YTT during the MIS 5-MIS 4 transition, and eruption 14 during the MIS 4-MIS 3 transition.

We propose a dual impact of such large explosive events on surface seawater carbonate chemistry. Short-term acidification, as evidenced by a decrease in surface seawater pH, in calcification intensity of *G. ruber*, and in sediment $CaCO_3$ accumulation, likely caused by sulphur emissions. Conversely, the observed pH increases after eruption events could be due to long-term alkalinization effect related to chemical weathering of large ash deposits on land. Future work will be needed to better constrain and understand the spatial extent of surface ocean acidification following the Toba eruptions.

Overall, our $\delta^{11}B$ data suggest direct or indirect effects of large explosive eruptions on the carbonate chemistry of surface marine waters (acidification and alkalinisation) and therefore on

the CO_2 budget, which calls for further studies on the scale of a giant volcanic complex like Toba.

Acknowledgements

We thank Sooriadea Dalliah and Lola Johannes (CR2P) for sampling and washing assistance of core material. We thank Sylvain Pont (IMPMC MNHN) for the acquisition of the SEM images of the planktic foraminifera. We thank Hélène Rebaubier, Patricia Richard, Morgane Fries, Fatima Manssouri and Gulay Isguder (LSCE) for analytical support. We thank Isabelle Billy (EPOC) for XRF analytical support. We thank Pierre Burckel, Pamela Gutiérrez (IPGP, ICP-MS), Tu-Han Luu and Dimitri Rigoussen (IPGP, MC-ICP-MS) for analytical support. We also thank Julien Bouchez (IPGP) for the fruitful discussion and advice on data processing and statistics.

Financial support

Financial support was provided by thesis grant from *Institut de l'Océan* (Sorbonne University), TALISMAN project (MNHN, Origins & Evolution Department) grant, CNRS INSU LEFE 2021 project ETOB grant, French National Research Agency (ANR) through the project B2SeaCarb (ANR-16-92CE-0010), IdEX Université Paris Cité ANR-18-IDEX-0001, IPGP multidisciplinary programme PARI, Paris-IdF Region SESAME grant n°12015908.

Data and materials availability

Data will be made available on request and on PANGAEA.

References

Barker, S., Greaves, M., Elderfield, H., 2003. A study of cleaning procedures used for foraminiferal Mg/Ca paleothermometry. Geochem. Geophys. Geosyst. 4, n/a-n/a. https://doi.org/10.1029/2003GC000559

Bereiter, B., Eggleston, S., Schmitt, J., Nehrbass-Ahles, C., Stocker, T.F., Fischer, H., Kipfstuhl, S., Chappellaz, J., 2015. Revision of the EPICA Dome C CO_2 record from 800 to 600 kyr before present: Analytical bias in the EDC CO2 record. Geophys. Res. Lett. 42, 542–549. https://doi.org/10.1002/2014GL061957

Börker, J., Hartmann, J., Romero-Mujalli, G., Li, G., 2019. Aging of basalt volcanic systems and decreasing CO2 consumption by weathering. Earth Surf. Dynam. 7, 191–197. https://doi.org/10.5194/esurf-7-191-2019

Buisson, M., Louvat, P., Thaler, C., Rollion-Bard, C., 2021. High precision MC-ICP-MS measurements of 11B/10B ratios from ng amounts of boron in carbonate samples using microsublimation and direct injection (μ-dDIHEN). J. Anal. At. Spectrom. 36, 2116–2131. https://doi.org/10.1039/D1JA00109D

Caron, B., Del Manzo, G., Villemant, B., Bartolini, A., Moreno, E., Le Friant, A., Bassinot, F., Baudin, F., Alves, A., 2023. Marine records reveal multiple phases of Toba's last volcanic activity. Sci Rep 13, 11575. https://doi.org/10.1038/s41598-023-37999-w

Catanzaro, E.J., 1970. Boric acid: isotopic and assay standard reference materials. National Bureau of Standards, Institute for Materials Research.

Chesner, C.A., 2012. The Toba Caldera Complex. Quaternary International 258, 5–18. https://doi.org/10.1016/j.quaint.2011.09.025

Costa, A., Smith, V.C., Macedonio, G., Matthews, N.E., 2014. The magnitude and impact of the Youngest Toba Tuff super-eruption. Front. Earth Sci. 2. https://doi.org/10.3389/feart.2014.00016

De La Vega, E., Chalk, T.B., Hain, M.P., Wilding, M.R., Casey, D., Gledhill, R., Luo, C., Wilson, P.A., Foster, G.L., 2023. Orbital CO_2 reconstruction using boron isotopes during the late Pleistocene, an assessment of accuracy (preprint). Proxy Use-Development-Validation/Marine Archives/Pleistocene. https://doi.org/10.5194/cp-2022-93

Dessert, C., Dupré, B., Gaillardet, J., François, L.M., Allègre, C.J., 2003. Basalt weathering laws and the impact of basalt weathering on the global carbon cycle. Chemical Geology 202, 257–273. https://doi.org/10.1016/j.chemgeo.2002.10.001

Doney, S.C., Mahowald, N., Lima, I., Feely, R.A., Mackenzie, F.T., Lamarque, J.-F., Rasch, P.J., 2007. Impact of anthropogenic atmospheric nitrogen and sulphur deposition on ocean acidification and the inorganic

carbon system. Proc. Natl. Acad. Sci. U.S.A. 104, 14580–14585. https://doi.org/10.1073/pnas.0702218104

Dong, S., Lei, Y., Bi, H., Xu, K., Li, T., Jian, Z., 2022. Biological Response of Planktic Foraminifera to Decline in Seawater pH. Biology 11, 98. https://doi.org/10.3390/biology11010098

Foster, G.L., 2008. Seawater pH, pCO2 and [CO2−3] variations in the Caribbean Sea over the last 130 kyr: A boron isotope and B/Ca study of planktic foraminifera. Earth and Planetary Science Letters 271, 254–266. https://doi.org/10.1016/j.epsl.2008.04.015

Foster, G.L., Pogge von Strandmann, P.A.E., Rae, J.W.B., 2010. Boron and magnesium isotopic composition of seawater: DATA BRIEF. Geochem. Geophys. Geosyst. 11, n/a-n/a. https://doi.org/10.1029/2010GC003201

Gaillardet, J., Dupré, B., Louvat, P., Allègre, C.J., 1999. Global silicate weathering and CO2 consumption rates deduced from the chemistry of large rivers. Chemical Geology 159, 3–30. https://doi.org/10.1016/S0009-2541(99)00031-5

Gaillardet, J., Lemarchand, D., Göpel, C., Manhès, G., 2001. Evaporation and Sublimation of Boric Acid: Application for Boron Purification from Organic Rich Solutions. Geostandards and Geoanalytical Research 25, 67–75. https://doi.org/10.1111/j.1751-908X.2001.tb00788.x

Gray, W.R., Evans, D., 2019. Nonthermal Influences on Mg/Ca in Planktonic Foraminifera: A Review of Culture Studies and Application to the Last Glacial Maximum. Paleoceanography and Paleoclimatology 34, 306–315. https://doi.org/10.1029/2018PA003517

Gray, W.R., Weldeab, S., Lea, D.W., Rosenthal, Y., Gruber, N., Donner, B., Fischer, G., 2018. The effects of temperature, salinity, and the carbonate system on Mg/Ca in Globigerinoides ruber (white): A global sediment trap calibration. Earth and Planetary Science Letters 482, 607–620. https://doi.org/10.1016/j.epsl.2017.11.026

Guillermic, M., Misra, S., Eagle, R., Villa, A., Chang, F., Tripati, A., 2020. Seawater pH reconstruction using boron isotopes in multiple planktonic foraminifera species with different depth habitats and their potential to constrain pH and CO2 gradients. Biogeosciences 17, 3487–3510. https://doi.org/10.5194/bg-17-3487-2020

Hathorne, E.C., Gagnon, A., Felis, T., Adkins, J., Asami, R., Boer, W., Caillon, N., Case, D., Cobb, K.M., Douville, E., deMenocal, P., Eisenhauer, A., Garbe-Schönberg, D., Geibert, W., Goldstein, S., Hughen, K., Inoue, M., Kawahata, H., Kölling, M., Cornec, F.L., Linsley, B.K., McGregor, H.V., Montagna, P.,

Nurhati, I.S., Quinn, T.M., Raddatz, J., Rebaubier, H., Robinson, L., Sadekov, A., Sherrell, R., Sinclair, D., Tudhope, A.W., Wei, G., Wong, H., Wu, H.C., You, C.-F., 2013. Interlaboratory study for coral Sr/Ca and other element/Ca ratio measurements. Geochem. Geophys. Geosyst. 14, 3730–3750. https://doi.org/10.1002/ggge.20230

Henehan, M.J., Evans, D., Shankle, M., Burke, J.E., Foster, G.L., Anagnostou, E., Chalk, T.B., Stewart, J.A., Alt, C.H.S., Durrant, J., Hull, P.M., 2017. Size-dependent response of foraminiferal calcification to seawater carbonate chemistry. Biogeosciences 14, 3287–3308. https://doi.org/10.5194/bg-14-3287-2017

Henehan, M.J., Foster, G.L., Bostock, H.C., Greenop, R., Marshall, B.J., Wilson, P.A., 2016. A new boron isotope-pH calibration for Orbulina universa, with implications for understanding and accounting for 'vital effects.' Earth and Planetary Science Letters 454, 282–292. https://doi.org/10.1016/j.epsl.2016.09.024

Henehan, M.J., Rae, J.W.B., Foster, G.L., Erez, J., Prentice, K.C., Kucera, M., Bostock, H.C., Martínez-Botí, M.A., Milton, J.A., Wilson, P.A., Marshall, B.J., Elliott, T., 2013. Calibration of the boron isotope proxy in the planktonic foraminifera Globigerinoides ruber for use in palaeo-CO2 reconstruction. Earth and Planetary Science Letters 364, 111–122. https://doi.org/10.1016/j.epsl.2012.12.029

Hönisch, B., Hemming, N.G., 2005. Surface ocean pH response to variations in pCO2 through two full glacial cycles. Earth and Planetary Science Letters 236, 305–314. https://doi.org/10.1016/j.epsl.2005.04.027

Hönisch, B., Ridgwell, A., Schmidt, D.N., Thomas, E., Gibbs, S.J., Sluijs, A., Zeebe, R., Kump, L., Martindale, R.C., Greene, S.E., Kiessling, W., Ries, J., Zachos, J.C., Royer, D.L., Barker, S., Marchitto, T.M., Moyer, R., Pelejero, C., Ziveri, P., Foster, G.L., Williams, B., 2012. The Geological Record of Ocean Acidification. Science 335, 1058–1063. https://doi.org/10.1126/science.1208277

Jones, M.T., Hembury, D.J., Palmer, M.R., Tonge, B., Darling, W.G., Loughlin, S.C., 2011. The weathering and element fluxes from active volcanoes to the oceans: a Montserrat case study. Bull Volcanol 73, 207–222. https://doi.org/10.1007/s00445-010-0397-0

Jouini, A., Paris, G., Caro, G., Bartolini, A., Gardin, S., 2023. Constraining oceanic carbonate chemistry evolution during the Cretaceous-Paleogene transition: Combined benthic and planktonic calcium isotope records from the equatorial Pacific Ocean. Earth and Planetary Science Letters 619, 118305. https://doi.org/10.1016/j.epsl.2023.118305

Jurikova, H., Liebetrau, V., Gutjahr, M., Rollion-Bard, C., Hu, M.Y., Krause, S., Henkel, D., Hiebenthal, C., Schmidt, M., Laudien, J., Eisenhauer, A., 2019. Boron isotope systematics of cultured brachiopods:

754 Response to acidification, vital effects and implications for palaeo-pH reconstruction. Geochimica et
755 Cosmochimica Acta 248, 370–386. https://doi.org/10.1016/j.gca.2019.01.015
756 Klochko, K., Kaufman, A.J., Yao, W., Byrne, R.H., Tossell, J.A., 2006. Experimental measurement of boron
757 isotope fractionation in seawater. Earth and Planetary Science Letters 248, 276–285.
758 https://doi.org/10.1016/j.epsl.2006.05.034
759 Lane, C.S., Chorn, B.T., Johnson, T.C., 2013. Ash from the Toba supereruption in Lake Malawi shows no
760 volcanic winter in East Africa at 75 ka. Proc. Natl. Acad. Sci. U.S.A. 110, 8025–8029.
761 https://doi.org/10.1073/pnas.1301474110
762 Langmann, B., 2014. On the Role of Climate Forcing by Volcanic Sulphate and Volcanic Ash. Advances in
763 Meteorology 2014, 1–17. https://doi.org/10.1155/2014/340123
764 Lemarchand, D., Gaillardet, J., Lewin, É., Allègre, C.J., 2002. Boron isotope systematics in large rivers:
765 implications for the marine boron budget and paleo-pH reconstruction over the Cenozoic. Chemical
766 Geology 190, 123–140. https://doi.org/10.1016/S0009-2541(02)00114-6
767 Lisiecki, L.E., Stern, J.V., 2016. Regional and global benthic δ^{18}O stacks for the last glacial cycle: Last Glacial
768 Cycle Benthic δ^{18}O. Paleoceanography 31, 1368–1394. https://doi.org/10.1002/2016PA003002
769 Louvat, P., Allègre, C.J., 1997. Present denudation rates on the island of Réunion determined by river
770 geochemistry: Basalt weathering and mass budget between chemical and mechanical erosions.
771 Geochimica et Cosmochimica Acta 61, 3645–3669. https://doi.org/10.1016/S0016-7037(97)00180-4
772 Louvat, P., Bouchez, J., Paris, G., 2011. MC-ICP-MS Isotope Measurements with Direct Injection Nebulisation
773 (d-DIHEN): Optimisation and Application to Boron in Seawater and Carbonate Samples. Geostandards
774 and Geoanalytical Research 35, 75–88. https://doi.org/10.1111/j.1751-908X.2010.00057.x
775 Louvat, P., Moureau, J., Paris, G., Bouchez, J., Noireaux, J., Gaillardet, J., 2014. A fully automated direct
776 injection nebulizer (d-DIHEN) for MC-ICP-MS isotope analysis: application to boron isotope ratio
777 measurements. J. Anal. At. Spectrom. 29, 1698–1707. https://doi.org/10.1039/C4JA00098F
778 Louvat, P., Tharaud, M., Buisson, M., Rollion-Bard, C., Benedetti, M.F., 2019. µ-dDIHEN: a new micro-flow
779 liquid sample introduction system for direct injection nebulization in ICP-MS. J. Anal. At. Spectrom.
780 34, 1553–1563. https://doi.org/10.1039/C9JA00146H
781 Mark, D.F., Renne, P.R., Dymock, R.C., Smith, V.C., Simon, J.I., Morgan, L.E., Staff, R.A., Ellis, B.S., Pearce,
782 N.J.G., 2017. High-precision 40Ar/39Ar dating of pleistocene tuffs and temporal anchoring of the

783 Matuyama-Brunhes boundary. Quaternary Geochronology 39, 1–23.
784 https://doi.org/10.1016/j.quageo.2017.01.002
785 Martínez-Botí, M.A., Marino, G., Foster, G.L., Ziveri, P., Henehan, M.J., Rae, J.W.B., Mortyn, P.G., Vance, D.,
786 2015. Boron isotope evidence for oceanic carbon dioxide leakage during the last deglaciation. Nature
787 518, 219–222. https://doi.org/10.1038/nature14155
788 Misra, S., Greaves, M., Owen, R., Kerr, J., Elmore, A.C., Elderfield, H., 2014. Determination of B/Ca of natural
789 carbonates by HR-ICP-MS. Geochem. Geophys. Geosyst. 15, 1617–1628.
790 https://doi.org/10.1002/2013GC005049
791 Ninkovich, D., Shackleton, N.J., Abdel-Monem, A.A., Obradovich, J.D., Izett, G., 1978. K–Ar age of the late
792 Pleistocene eruption of Toba, north Sumatra. Nature 276, 574–577. https://doi.org/10.1038/276574a0
793 Oppenheimer, C., 2002. Limited global change due to the largest known Quaternary eruption, Toba ≈74kyr BP?
794 Quaternary Science Reviews 21, 1593–1609. https://doi.org/10.1016/S0277-3791(01)00154-8
795 Petit, J.R., Jouzel, J., Raynaud, D., Barkov, N.I., Barnola, J.-M., Basile, I., Bender, M., Chappellaz, J., Davis, M.,
796 Delaygue, G., Delmotte, M., Kotlyakov, V.M., Legrand, M., Lipenkov, V.Y., Lorius, C., PÉpin, L.,
797 Ritz, C., Saltzman, E., Stievenard, M., 1999. Climate and atmospheric history of the past 420,000 years
798 from the Vostok ice core, Antarctica. Nature 399, 429–436. https://doi.org/10.1038/20859
799 Rae, J.W.B., Foster, G.L., Schmidt, D.N., Elliott, T., 2011. Boron isotopes and B/Ca in benthic foraminifera:
800 Proxies for the deep ocean carbonate system. Earth and Planetary Science Letters 302, 403–413.
801 https://doi.org/10.1016/j.epsl.2010.12.034
802 Raitzsch, M., Bijma, J., Benthien, A., Richter, K.-U., Steinhoefel, G., Kučera, M., 2018. Boron isotope-based
803 seasonal paleo-pH reconstruction for the Southeast Atlantic – A multispecies approach using habitat
804 preference of planktonic foraminifera. Earth and Planetary Science Letters 487, 138–150.
805 https://doi.org/10.1016/j.epsl.2018.02.002
806 Rampino, M.R., Self, S., 1992. Volcanic winter and accelerated glaciation following the Toba super-eruption.
807 Nature 359, 50–52. https://doi.org/10.1038/359050a0
808 Rivé, K., Gaillardet, J., Agrinier, P., Rad, S., 2013. Carbon isotopes in the rivers from the Lesser Antilles: origin
809 of the carbonic acid consumed by weathering reactions in the Lesser Antilles. Earth Surf. Process.
810 Landforms 38, 1020–1035. https://doi.org/10.1002/esp.3385
811 Robock, A., 2000. Volcanic eruptions and climate. Rev. Geophys. 38, 191–219.
812 https://doi.org/10.1029/1998RG000054

Rose, W.I., Chesner, C.A., 1990. Worldwide dispersal of ash and gases from earth's largest known eruption: Toba, Sumatra, 75 ka. Palaeogeography, Palaeoclimatology, Palaeoecology 89, 269–275. https://doi.org/10.1016/0031-0182(90)90068-I

Sanyal, A., Hemming, N.G., Hanson, G.N., Broecker, W.S., 1995. Evidence for a higher pH in the glacial ocean from boron isotopes in foraminifera. Nature 373, 234–236. https://doi.org/10.1038/373234a0

Sarma, V.V.S.S., Narvekar, P.V., 2001. A study on inorganic carbon components in the Andaman Sea during the post monsoon season. Oceanologica Acta 24, 125–134. https://doi.org/10.1016/S0399-1784(00)01133-6

Schiebel, R., Smart, S.M., Jentzen, A., Jonkers, L., Morard, R., Meilland, J., Michel, E., Coxall, H.K., Hull, P.M., De Garidel-Thoron, T., Aze, T., Quillévéré, F., Ren, H., Sigman, D.M., Vonhof, H.B., Martínez-García, A., Kučera, M., Bijma, J., Spero, H.J., Haug, G.H., 2018. Advances in planktonic foraminifer research: New perspectives for paleoceanography. Revue de Micropaléontologie 61, 113–138. https://doi.org/10.1016/j.revmic.2018.10.001

Schulz, H., Emeis, K.-C., Erlenkeuser, H., Von Rad, U., Rolf, C., 2002. The Toba Volcanic Event and Interstadial/Stadial Climates at the Marine Isotopic Stage 5 to 4 Transition in the Northern Indian Ocean. Quat. res. 57, 22–31. https://doi.org/10.1006/qres.2001.2291

Shao, J., Stott, L.D., Gray, W.R., Greenop, R., Pecher, I., Neil, H.L., Coffin, R.B., Davy, B. and Rae, J.W.B. (2019), Atmosphere-Ocean CO2 Exchange Across the Last Deglaciation From the Boron Isotope Proxy. Paleoceanography and Paleoclimatology, 34: 1650-1670. https://doi.org/10.1029/2018PA003498

Smith, E.I., Jacobs, Z., Johnsen, R., Ren, M., Fisher, E.C., Oestmo, S., Wilkins, J., Harris, J.A., Karkanas, P., Fitch, S., Ciravolo, A., Keenan, D., Cleghorn, N., Lane, C.S., Matthews, T., Marean, C.W., 2018. Humans thrived in South Africa through the Toba eruption about 74,000 years ago. Nature 555, 511–515. https://doi.org/10.1038/nature25967

Spratt, R.M., Lisiecki, L.E., 2016. A Late Pleistocene sea level stack. Clim. Past 12, 1079–1092. https://doi.org/10.5194/cp-12-1079-2016

Stewart, J.A., Christopher, S.J., Kucklick, J.R., Bordier, L., Chalk, T.B., Dapoigny, A., Douville, E., Foster, G.L., Gray, W.R., Greenop, R., Gutjahr, M., Hemsing, F., Henehan, M.J., Holdship, P., Hsieh, Y., Kolevica, A., Lin, Y., Mawbey, E.M., Rae, J.W.B., Robinson, L.F., Shuttleworth, R., You, C., Zhang, S., Day, R.D., 2021. NIST RM 8301 Boron Isotopes in Marine Carbonate (Simulated Coral and Foraminifera Solutions): Inter-laboratory δ^{11}B and Trace Element Ratio Value Assignment. Geostand Geoanal Res 45, 77–96. https://doi.org/10.1111/ggr.12363

Storey, M., Roberts, R.G., Saidin, M., 2012. Astronomically calibrated ^{40}Ar/^{39}Ar age for the Toba supereruption and global synchronization of late Quaternary records. Proc. Natl. Acad. Sci. U.S.A. 109, 18684–18688. https://doi.org/10.1073/pnas.1208178109

van der Kaars, S., Williams, M.A.J., Bassinot, F., Guichard, F., Moreno, E., Dewilde, F., Cook, E.J., 2012. The influence of the ~73 ka Toba super-eruption on the ecosystems of northern Sumatra as recorded in marine core BAR94-25. Quaternary International 258, 45–53. https://doi.org/10.1016/j.quaint.2011.09.006

Vogl, J., Rosner, M., 2012. Production and Certification of a Unique Set of Isotope and Delta Reference Materials for Boron Isotope Determination in Geochemical, Environmental and Industrial Materials. Geostandards and Geoanalytical Research 36, 161–175. https://doi.org/10.1111/j.1751-908X.2011.00136.x

Waelbroeck, C., Labeyrie, L., Michel, E., Duplessy, J.C., McManus, J.F., Lambeck, K., Balbon, E., Labracherie, M., 2002. Sea-level and deep water temperature changes derived from benthic foraminifera isotopic records. Quaternary Science Reviews 21, 295–305. https://doi.org/10.1016/S0277-3791(01)00101-9

Weinkauf et al. 2013. Calcification intensity in planktonic Foraminifera reflects ambient conditions irrespective of environmental stress. Biogeosciences, 10, 6639–6655, 2013. www.biogeosciences.net/10/6639/2013/ doi:10.5194/bg-10-6639-2013

Westerhold, T., Röhl, U., McCarren, H.K., Zachos, J.C., 2009. Latest on the absolute age of the Paleocene–Eocene Thermal Maximum (PETM): New insights from exact stratigraphic position of key ash layers + 19 and − 17. Earth and Planetary Science Letters 287, 412–419. https://doi.org/10.1016/j.epsl.2009.08.027

Wolff-Boenisch, D., Gislason, S.R., Oelkers, E.H., 2006. The effect of crystallinity on dissolution rates and CO2 consumption capacity of silicates. Geochimica et Cosmochimica Acta 70, 858–870. https://doi.org/10.1016/j.gca.2005.10.016

Yu, J., Day, J., Greaves, M., Elderfield, H., 2005. Determination of multiple element/calcium ratios in foraminiferal calcite by quadrupole ICP-MS. Geochem. Geophys. Geosyst. 6, n/a-n/a. https://doi.org/10.1029/2005GC000964

Zeebe, R.E., 2012. History of Seawater Carbonate Chemistry, Atmospheric CO_2, and Ocean Acidification. Annu. Rev. Earth Planet. Sci. 40, 141–165. https://doi.org/10.1146/annurev-earth-042711-105521

Supplementary Materials for

Sea surface acidification events in the Andaman Sea associated with the last Toba volcanic activity

Ana Alves* *et al.*

*Corresponding author. Email: ana.alves@mnhn.fr

This PDF file includes:

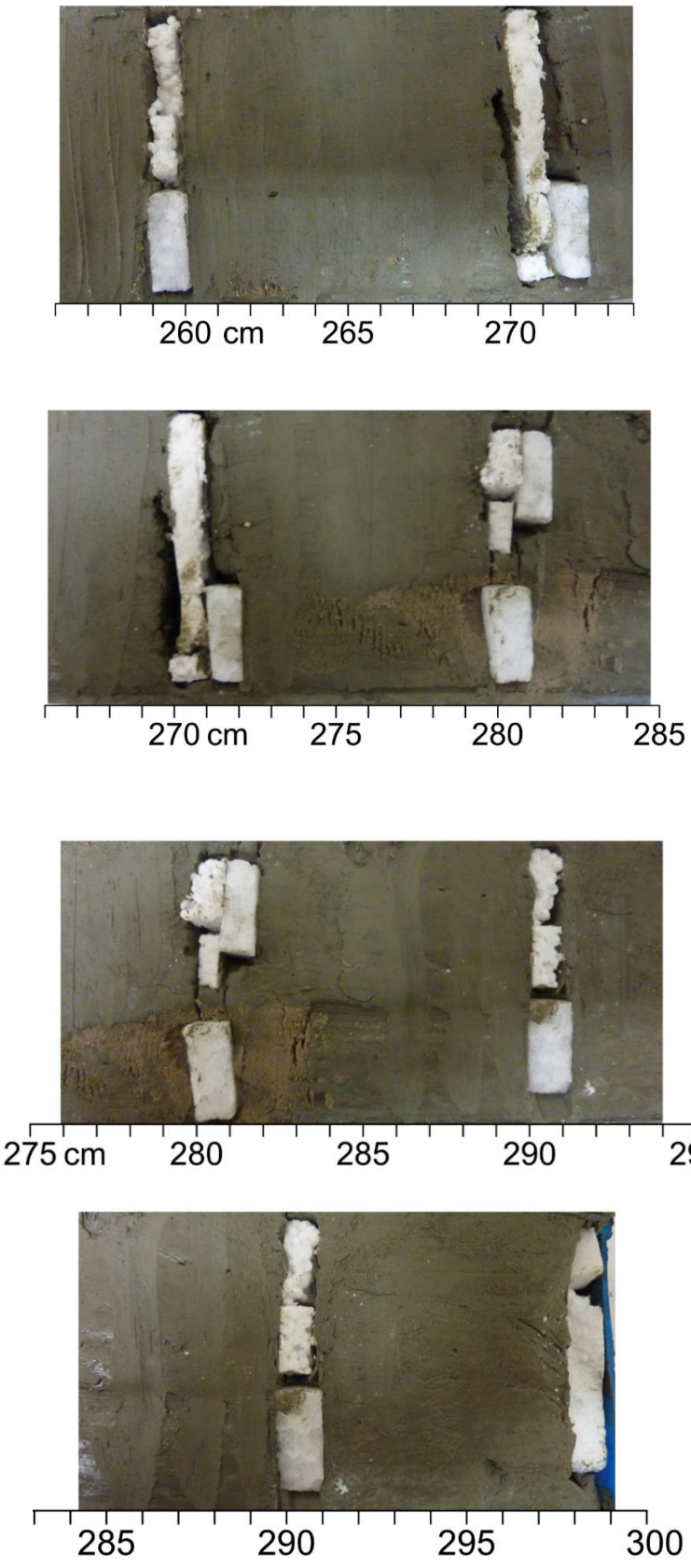

Fig. S1. Photography of section 2 of core BAR94-25 (from 256 to 299 cm depth). The tephra layer 14, which has a nodular appearance, is clearly visible from 275 cm to 284 cm.

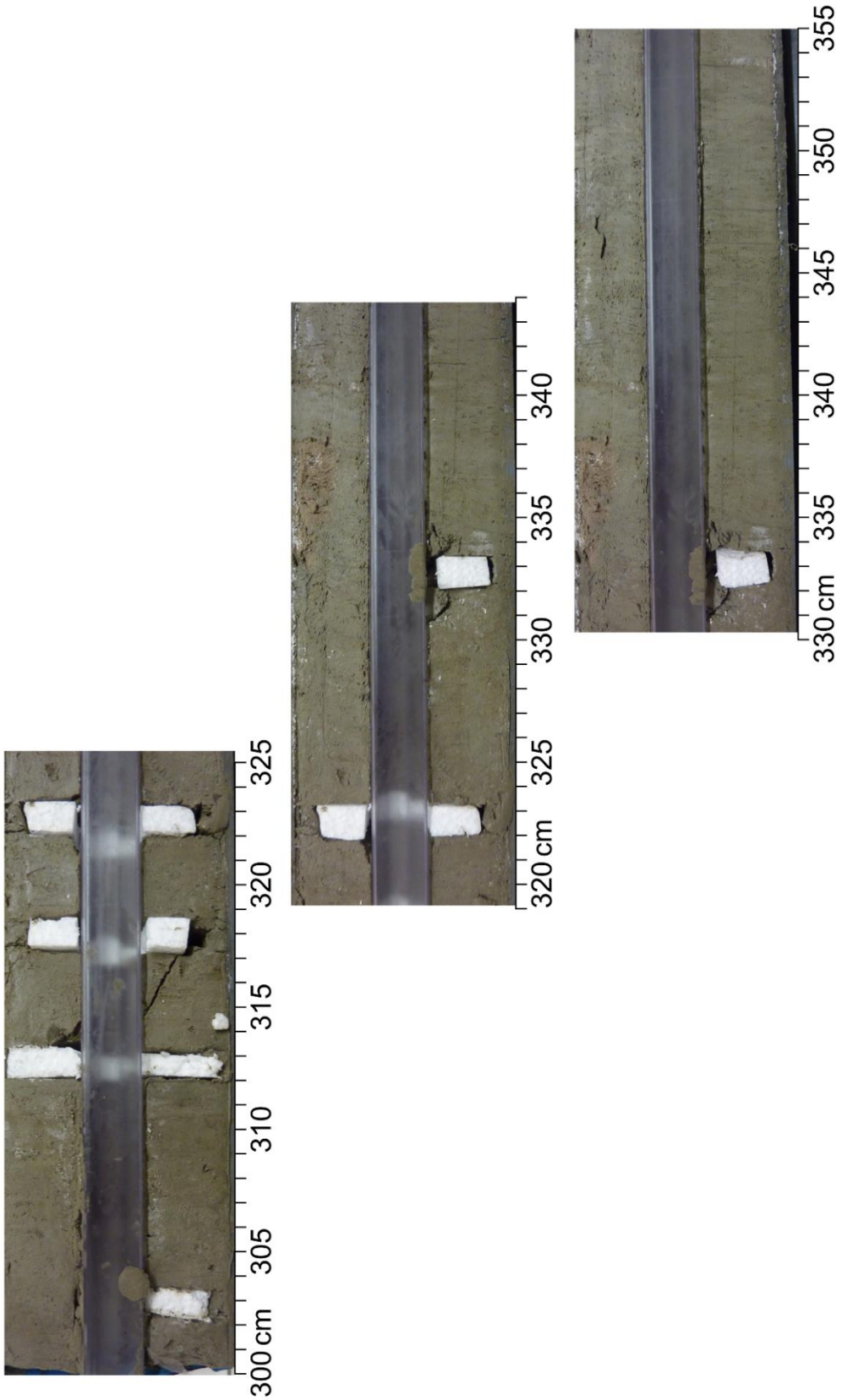

Fig. S2. Photography of section 3 of core BAR94-25 (from 300 to 355 cm depth). From 309 to 318 cm is the tephra layer 10, considered as the YTT.

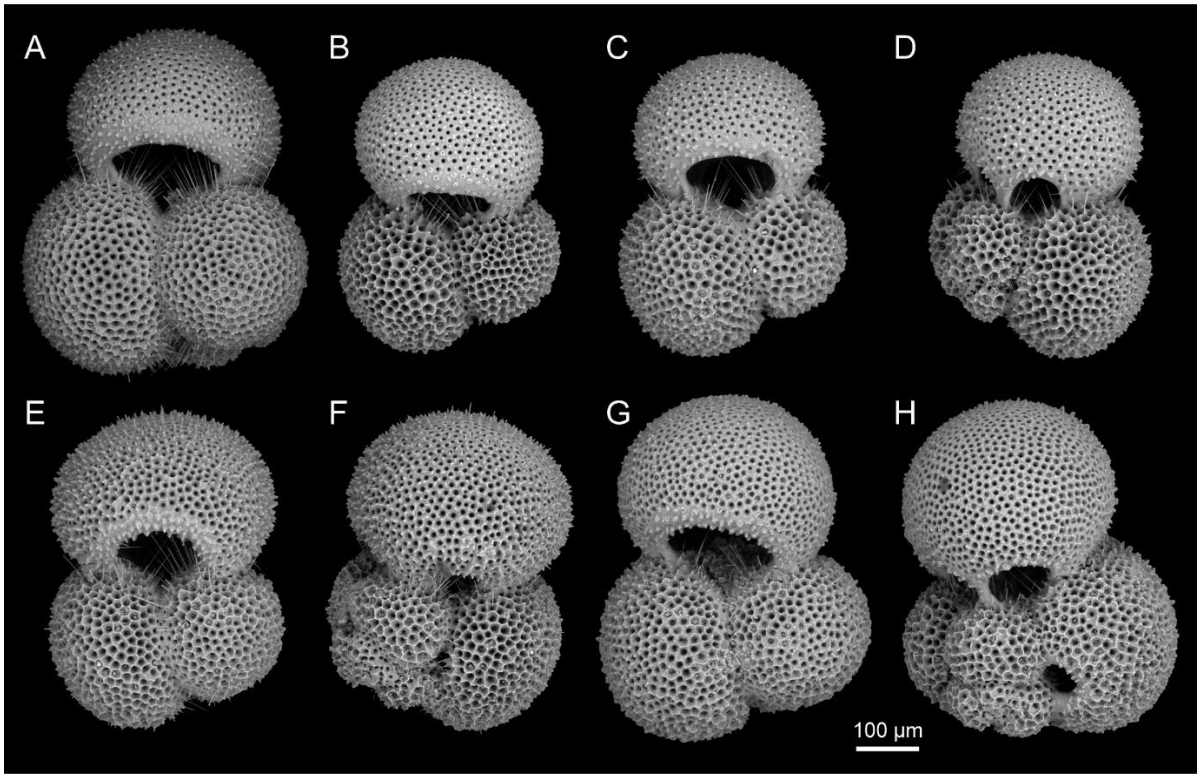

Fig. S3. Scanning electron microscope (SEM)/backscattered electron (BSE) images of several specimens of *Globigerinoides ruber* s.s. (d'Orbigny, 1839) from the Toba tephra layer number 10 of marine core BAR94-25. The specimens show a pristine, unaltered surface texture with no signs of dissolution or authigenic overgrowth crystals, and delicate structures such as spines are present: (A) specimen from 317 cm depth, umbilical side view; (B) specimen from 314 cm depth, umbilical side view; (C) specimen from 316 cm depth, umbilical side view; (D) same specimen as C, dorsal side view; (E) specimen from 315 cm depth, umbilical side view; (F) same specimen as E, dorsal side view; (G) specimen from 313 cm depth, umbilical side view; (H) same specimen as G, dorsal side view.

1. Age model

Core BAR94-25 has several ash layers that were identified during previous studies (Caron et al., 2023). These layers correspond to rapid deposits of ashes (tephra and cryptotephra) after the several eruptions of Toba volcano. The sedimentation rate is consequently modified during these events and it can significantly impact the age model. A way to avoid this perturbation is to tighten the record along the core. To do so, we decided to use the record of $CaCO_3$ content of the core that is directly impacted by the contribution of ashes. The $CaCO_3$ content varies from 35 to 20% along the core. When there is an important deposit of ashes, the $CaCO_3$ content is diluted and the percentage falls under 20%, with a minimum of 7% at 282 cm whereas the K/Ti ratio increases. In order to correct the sedimentation rate, we choose to tighten the record where these drops of $CaCO_3$ content happened. The same depth is therefore attributed to several points (Fig. S4, in red) that represent the instantaneous input of ashes and subtract the depth interval concerned to the rest of the core. At the end of this step, 13 cm were subtracted to the core depth. The new depths (depth corrected) were then transferred to all the records included the $\delta^{18}O$ that is used for the age model.

We improved the existing $\delta^{18}O$-derived age model of BAR94-25, taking advantage of the higher-resolution interval and using a different approach than van der Kaars *et al.* (van der Kaars et al., 2012). We used as a reference record, core MD98-2165 from the Eastern Indian Ocean (South of Indonesia). This core has a robust age model (Pang et al., 2021), based on ^{14}C dates and the tuning of its benthic $\delta^{18}O$ record to the benthic $\delta^{18}O$ LS16 regional reference record of Lisiecki and Stern (Lisiecki and Stern, 2016). We then transferred this globally coherent benthic-derived age model to core BAR94-25 by visually tuning the BAR94-25 $\delta^{18}O$ planktonic record, with the new depths, to the MD98-2165 planktonic $\delta^{18}O$ record (Fig. S5)

using QAnalyseries software (Kotov and Pälike, 2018). Depth to age conversion was achieved through linear interpolation between 20 tie-points (Table S1).

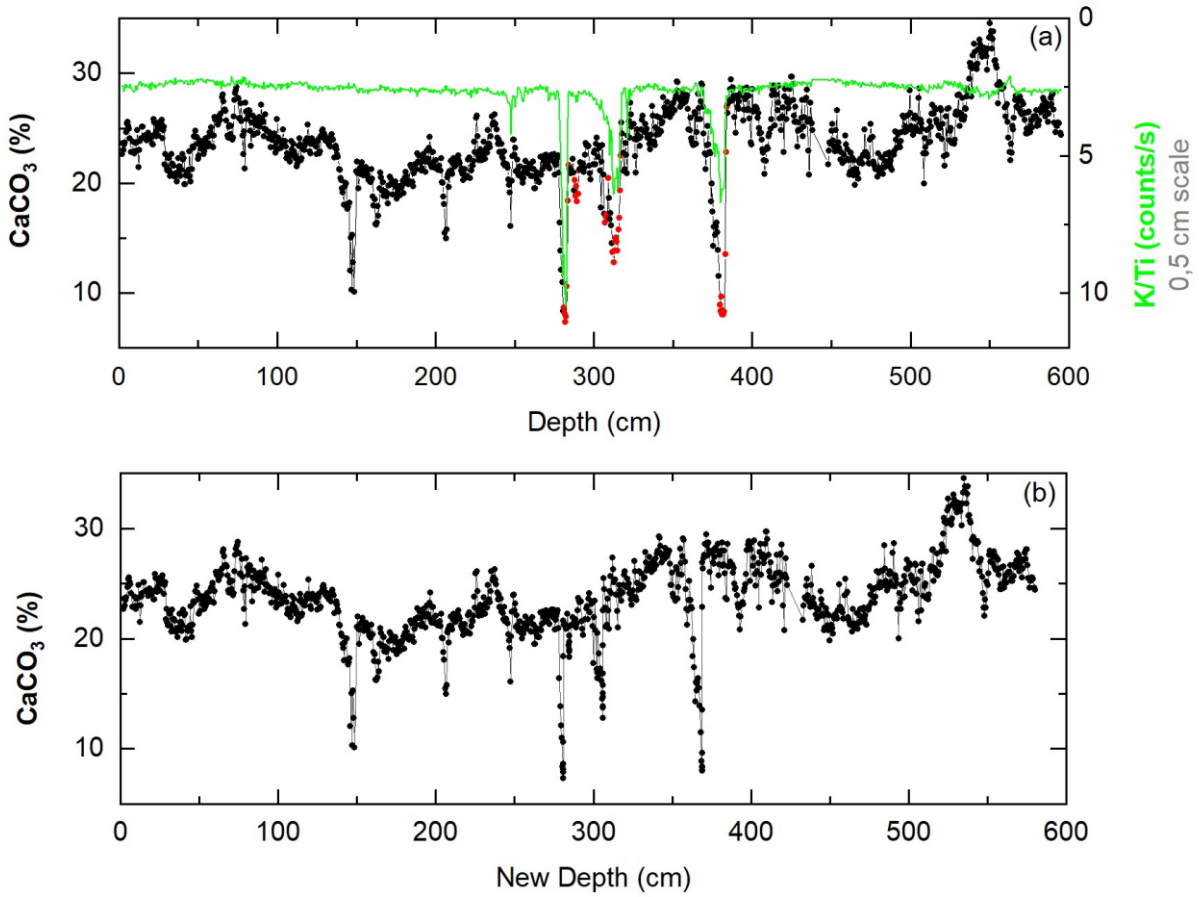

Fig. S4. Tightening of the $CaCO_3$ record of core BAR94-25 according to the deposit of ashes by Toba volcano. (a), $CaCO_3$ content (black) and ratio K/Ti (green, inverted scale) of core BAR94-25 with the initial depth. The red dots represent the intervals where $CaCO_3$ content falls due to deposit of ashes along the core. (b), $CaCO_3$ content of core BAR95-25 with the new depth (after the tightening).

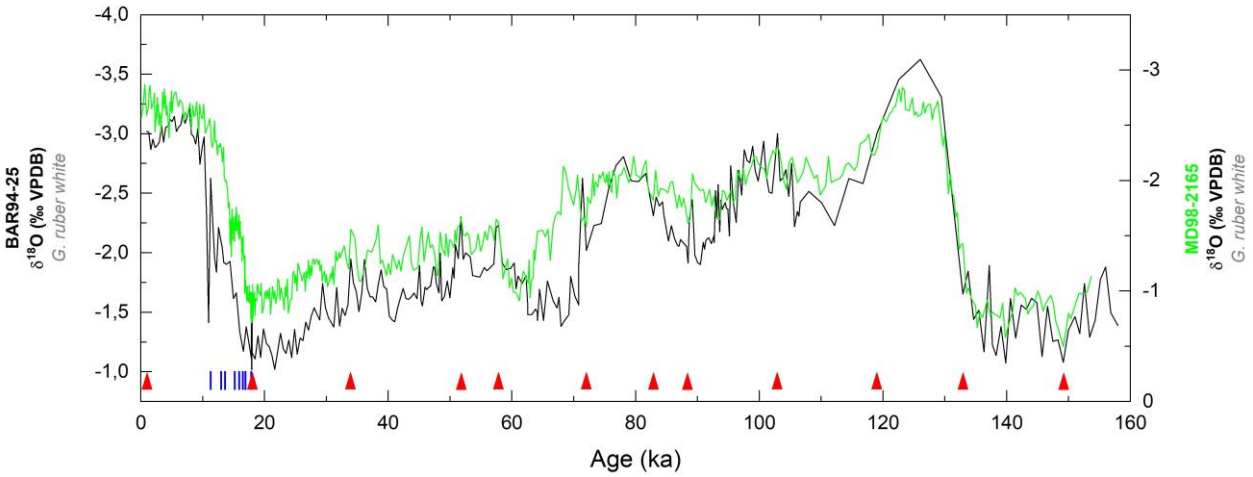

Fig. S5. Age model of core BAR94-25. Tuning of the BAR94-25 $\delta^{18}O$ planktonic record (black) with the MD98-2165 $\delta^{18}O$ planktonic record (green). Red triangles indicate the tie points between the two records and blue lines indicate the ^{14}C calendar dates of core MD98-2165.

New depth BAR94-25 (cm)	Age (ka)	Type
0	0,91	$\delta^{18}O$ planktonic
61	11,45	$\delta^{18}O$ planktonic
70	12,91	$\delta^{18}O$ planktonic
75	13,56	$\delta^{18}O$ planktonic
80	14,93	$\delta^{18}O$ planktonic
84	15,83	$\delta^{18}O$ planktonic
86	16,46	$\delta^{18}O$ planktonic
88	16,92	$\delta^{18}O$ planktonic
89	17,86	$\delta^{18}O$ planktonic
100	18,01	$\delta^{18}O$ planktonic
170	33,93	$\delta^{18}O$ planktonic
250	51,76	$\delta^{18}O$ planktonic
266	57,84	$\delta^{18}O$ planktonic
311	72,04	$\delta^{18}O$ planktonic
329	82,84	$\delta^{18}O$ planktonic
352	88,46	$\delta^{18}O$ planktonic
417	102,91	$\delta^{18}O$ planktonic
487	119,08	$\delta^{18}O$ planktonic
527	132,91	$\delta^{18}O$ planktonic
717	149,16	$\delta^{18}O$ planktonic

Table S1. Tie points used for correlating MD98-2165 and BAR94-25 $\delta^{18}O$ records in order to establish the age model of the study core.

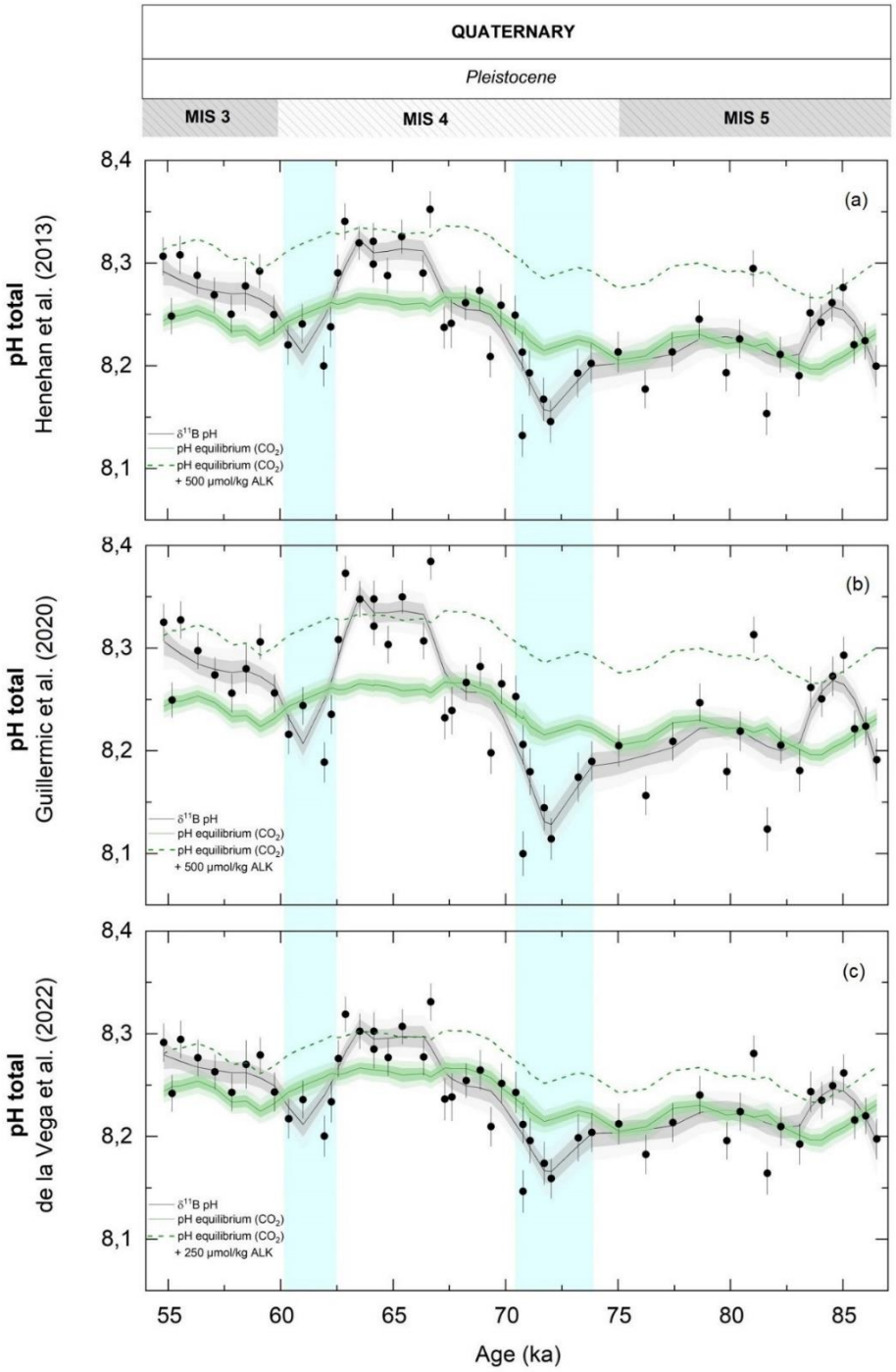

Fig. S6. pH reconstruction using different calibrations of the boron isotope proxy in the planktonic foraminifera *G. ruber*. (a), Henehan *et al.* (Henehan et al., 2013) calibration. (b), Guillermic *et al.* (Guillermic et al., 2020) calibration. (c), de la Vega *et al.* (De La Vega et al., 2023) calibration that corresponds to an optimized calibration of Henehan *et al.* (Henehan et al., 2013).

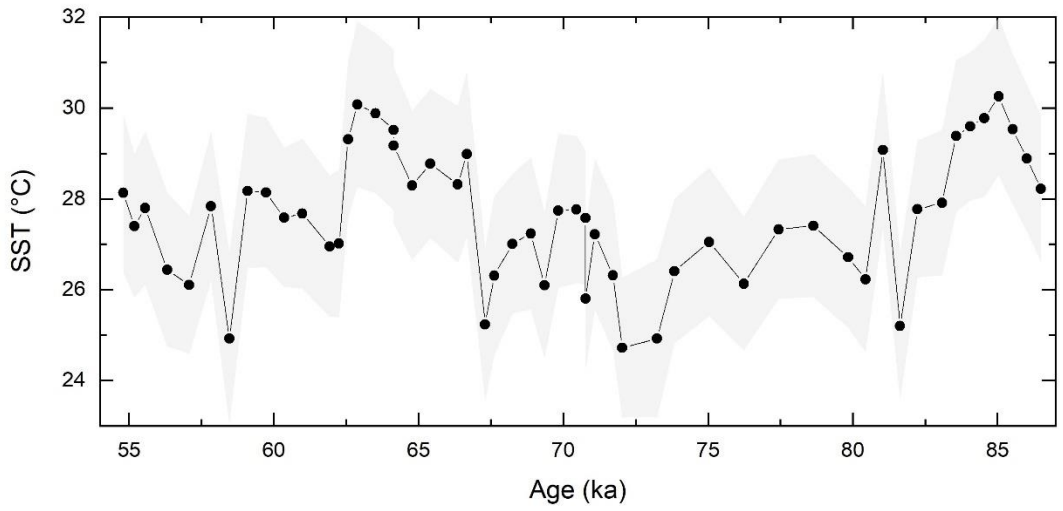

990

991 **Fig. S7.** Sea surface temperature of the Andaman Sea and 2σ uncertainty (gray), reconstructed
992 using Mg/Ca of *G. ruber* and the MgCaRB software package developed by Gray & Evans (Gray
993 and Evans, 2019).

994

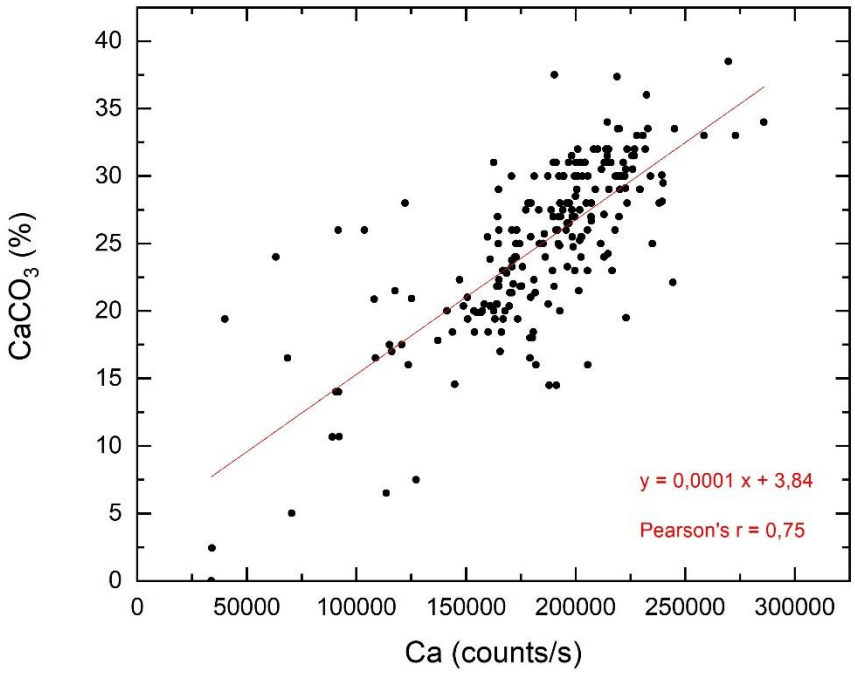

995

996 **Fig. S8.** Linear regression equation (Pearson correlation = 0.75) between $CaCO_3$ measurements
997 and XRF-measured Ca.

998

2. Boron isotope record from BAR94-25 marine core unaffected by contamination

The removal of clays is generally considered as effective when the Al/Ca ratio is lower than 100 µmol/mol (Rae et al., 2011). For Mn/Ca, the accepted threshold value for properly cleaned samples varies from 30 µmol/mol (Martin and Lea, 2002) to 80 µmol/mol (Raitzsch et al., 2018). Almost all Al/Ca values are below the threshold of 100µmol/mol (Gutjahr et al., 2017; Rae et al., 2011) and there is no relationship between Al/Ca and $\delta^{11}B$ for the entire data set, allowing to rule out the influence of clay contaminants on boron isotopic composition. Mn/Ca ratios ranges from ~280 to 540 µmol/mol, which is well above the established thresholds. The presence of oxide coatings would lead to enriched ^{10}B isotopic signatures (Lemarchand et al., 2007), but this is not the case here as there is also no relationship between the Mn/Ca ratio and $\delta^{11}B$. Mn content could rather reflect the availability in seawater of Mn^{2+} that can be incorporated during biocalcification. Indeed, ash falls during Toba eruption released bioactive metal in ocean surface water, leading to Zn and Mn enrichment in foraminifera tests from ash layers (Lemelle et al., 2020). XRF nanomapping of planktonic foraminiferal tests from the YTT layers on the same core as this study showed that the Mn enrichments in the foraminiferal tests are not in the form of a diagenetic coating but are incorporated according to their growth structures (Lemelle et al., 2020). This suggests that the high Mn/Ca observed in our samples is due to the incorporation of Mn^{2+} to biocalcification during the volcanic events. In summary, the lack of correlation with tracers of contamination during diagenesis or sample preparation suggests that the environmental signal of boron isotopes is well preserved.

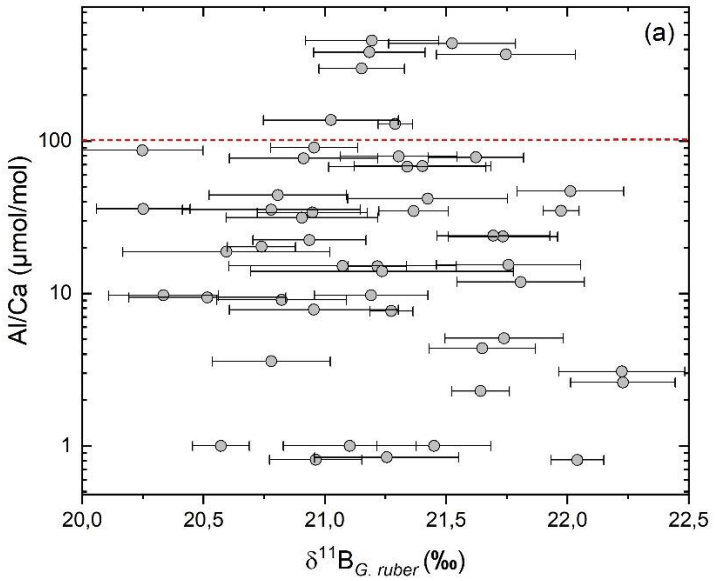

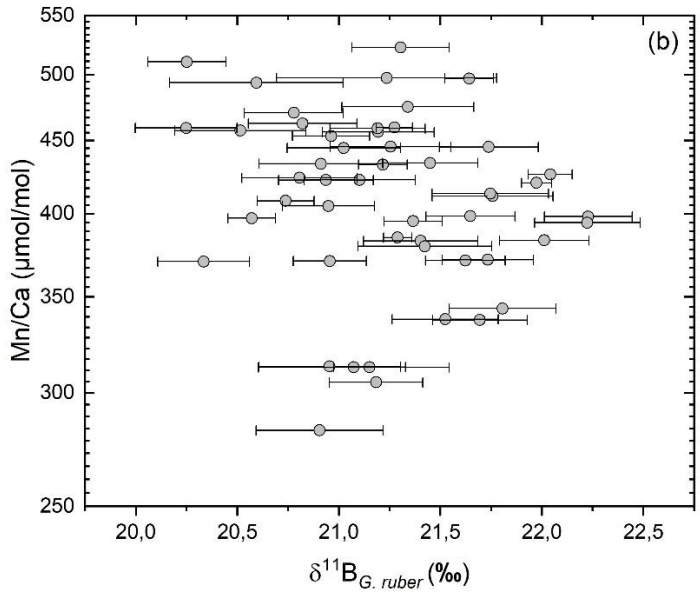

Fig. S9. Relationship between the $\delta^{11}B$ measured in *G. ruber* samples and the contamination indices. (a), Al/Ca ratio with the dotted red line that corresponds to the threshold accepted by Rae et al. (Rae et al., 2011). (b), Mn/Ca ratios. The objective is to see if the removal of organic matter and clays was well done.

3. Estimation of the sulphur flux necessary to acidify the sea surface by 0.1 pH units

To estimate the mass of Sulphur needed to decrease the pH of the Andaman Sea surface, we need to know the volume of water affected. Since *Gobigerinoides ruber* lives at a water depth of up to 50 meters, corresponding with the mixed layer, the volume can be calculated by multiplying 50 meters by the surface area affected by pH change (~40,000 km^3 of seawater in the Andaman Sea). We calculated the increase in H^+ concentration for an oceanic pH decreasing by 0.1 units using the Excel file CO_2Sys_v3.0_Err (Pierrot et al., 2021), with a modern temperature set at 29°C, salinity at 32 and total alkalinity at 2195 µmol/kg. We then assumed that this excess of protons comes exclusively from the dissociation of sulphuric acid with 2 mol of H+ (protons) coming from the dissociation of 1 mol of sulfate (SO_4^{2-}).

pH	H+ (nmol/kgSW)
8.100	7.94
8.000	10

Table S2. Estimation of the H+ concentration variation for a pH decrease of 0.1 units.

	Andaman Sea	Global Ocean
Area (km^2)	797700	361000000
Water depth (km)	0.05	0.05
Water volume (km^3)	39885	1.81×10^7
∆H+ (nmol/kgSW)	2.06	2.06
∆H+ (nmol/kgSW)/2	1.03	1.03
Sulphur (mol)	4.10×10^7	1.86×10^{19}
Sulphur (kg)	4.06×10^6	1.84×10^9

Table S3. Estimation of the sulphur needed to acidify the sea surface by 0.1 pH units.

If we consider the residence time of water that is close to 10 years in the Andaman Sea mixed layer, the amount of sulphur needed to decrease the pH by 0.1 would be 4.06×10^6 kg. In the literature, the amount of sulphur emitted by the Toba eruption is estimated between 3.5×10^{10} and 3.3×10^{12} kg (Oppenheimer, 2002). Therefore, the amount of sulphur needed to cause an acidification of 0.1 pH unit in the Andaman Sea could be provided by the Toba eruption. Making the same estimations for the global ocean, we obtain a value of 1.84×10^9 kg of sulphur. This estimation is closer to the amount of sulphur emitted by the Toba eruption (Oppenheimer, 2002). Further studies on other cores in the Indian Ocean and elsewhere are needed to constrain the spatial extent of acidification.

4. Alkalinization of the Andaman Sea through the chemical weathering of the YTT

An increasing number of studies have addressed the chemical weathering of volcanic edifices, especially of basaltic or intermediate (andesitic) composition, and their important role on the long-term carbon cycle (e.g., reviews in Dessert et al, 2003; Li et al, 2016; Börker et al., 2019 or Jones et al, 2019). However, few studies have investigated weathering process in the context of very acidic volcanism, preventing us from being able to provide an estimation of the weathering fluxes for the Younger Toba Tuffs, characterized by very acidic rhyolitic composition. Acidic volcanic rocks weather slower than basalts, as shown by laboratory or on-field experiments. For example, though and experimental dissolution studies, it was reported that rhyolites weathered 9 times slower than basalts (Wolff-Boenisch et al., 2004), and released also 5 times less Ca and 13 times less Mg than basalts (Olsson-Francis et al., 2012), while the initial rhyolite powder used contained 9 and 15 times less Ca and Mg than basalts. Contrastingly, at the scale of the watershed, it was shown for Sao Miguel, Azores, that river waters that drain basalts, intermediate or trachytic rocks have very similar weathering rates but different Ca/Na and Mg/Na ratios: higher for basaltic rivers and lower for trachytic rivers

(Louvat and Allègre, 1998), which is consistent with their chemical compositions. But these Ca/Na and Mg/Na molar ratios in the rivers are not as different as these ratios in the unweathered rocks of these watersheds: while Ca/Na and Mg/Na are respectively 7 and 5 times lower in the trachytic rivers compared to the basaltic rivers, they are 30, resp. 50, times lower in trachytes than in basalts. This underlines the non-congruent weathering of basalts and trachytes, which apparently favors Ca and Mg release from acidic volcanic rocks (relative to Na, considered as the most mobile cation during weathering). It is therefore difficult, if not impossible, to evaluate how rhyolite weathering will compare in terms of elemental weathering fluxes to basalt weathering. And we cannot just approportionate the basalt weathering rates with the rhyolite's chemical compositions. We can nonetheless attempt to evaluate weathering fluxes for the YTT.

Multiple studies have estimated weathering fluxes from volcanic islands (e.g. Louvat and Allègre 1997 and 1998, Louvat et al. 2008, Dessert et al., 2001, 2009, 2015; Rad et al, 2006, 2007, 2013; Goldsmith et al, 2008, 2010 et 2015; Jones et al, 2011; Gaillardet et al, 2011; Schopka et al., 2011; Eiriksdottir et al, 2008, 2013, 2015; Gislason et al., 1987, 1996, 2009; Carey et al., 2015; Harmon et al., 2016). Expressed as total dissolved solids times runoff (river annual discharge normalized to the surface area of the watershed), basalt weathering rate averages 100 $t/km^2/yr$ but is quite variable, from about 25 $t/km^2/yr$ in Azores to more than 1000 in Java (Louvat, 1997; Dessert et al., 2003). Associated Ca and Mg fluxes for Réunion, Azores, Iceland and Java average 0.31 and 0.19 x 10^6 $mol/km^2/yr$, respectively, and are also quite variable. On the one hand, the trachytic rivers in Azores deliver 0.04 x 10^6 $mol/km^2/yr$ for both Ca and Mg, only four times less than the basaltic rivers. On the other hand, Java rivers can discharge as high as 1 and 0.45 x 10^6 $mol/km^2/yr$ of Ca and Mg to the nearby ocean and sea (Louvat, 1997), due to higher temperature and intense precipitations. Thus, trachytic rivers on a given location tend to release less Ca than basaltic rivers (4 times in the case of the Azores),

but climate can induce dramatic differences in Ca delivery (10 times more for basaltic rivers on Java compared to Azores).

But if weathering rates vary according to the nature of the rocks, as seen in the previous paragraph for rhyolites and basalts, they also tend to decrease with aging of the rocks (Chadwick et al., 1999; Stewart et al., 2001; Gislason et al, 1996; Louvat et al., 2008; Gaillardet et al., 2011; Börker et al., 2018), the high porosity of young volcanic rocks enhancing the reactive surface areas (e.g. Welch et al., 2015) and thus water-rock interactions. For long timescales, the chemical weathering rate is for example 5 times lower for basalts or andesites more than 2 Myr old in Iceland (Louvat et al, 2008) or in Guadeloupe (Gaillardet et al., 2011), compared to younger rocks. Moreover, volcanic edifices are particularly porous and are true water towers, and even more so when they are young and the water drainage networks are not structured into a hydric network. Studies have determined that the fluxes from "underground" or "hidden" weathering could represent 30 to 100% of the weathering flux from volcanic islands such as Réunion, Guadeloupe, Martinique (Rad et al., 2007) or Hawaii (Shopka and Derry, 2012), underlying that the weathering of this highly permeable material is increased again. In conclusion, we assume than younger materials weather 5 times faster than older material.

In the present study, we are considering the weathering of young volcanic material emitted during Toba's paroxysmal activity phase (VAP2), including YTT. We assume that the increased weathering rate of these young porous tephra compared to older rocks compensates the reduced weathering rate of rhyolite compared to basalts. As a result of this approximation, fresh rhyolite will weather at rates similar to old basalt.

We make the further assumption that the weathering rates for Java basalts nowadays are transferable to Sumatra's Toba tephra 50-100 ka ago, we then extrapolate that today's weathering of old basalts on Java is the same as extremely fresh rhyolites on Sumatra after the YTT's emplacement. As a result, we can assume a weathering rate of about 1000 $t/km^2/yr$

(Louvat, 1997; Dessert et al., 2003). To be more specific, the elemental weathering fluxes for the basaltic rivers of Java are respectively 1, 0.45, 0.7 and 0.15 x 10^6 mol/km^2/yr for Ca, Mg, Na and K (Louvat, 1997). From these elemental fluxes, we can estimate the associated flux of alkalinity to the nearby seas, by summing the charge equivalent of these cation's fluxes and of the SO_4 flux, 2*Ca + 2*Mg + Na + K – 2*SO_4, amounting to 3.45 x 10^6 mol/km^2/yr of alkalinity. It should be noted that the fluxes given for Java's rivers only concern low-temperature basalt weathering, which means that they have been corrected for atmospheric and hydrothermal inputs to the rivers, and that Cl flux is therefore negligible (e.g. Louvat and Allègre 1998, 1999 or Louvat et al, 2006, for the correction method applied to Réunion, Azores or Iceland; not published for Java, but "total" weathering fluxes published in Dessert et al., 2003).

If we now consider that the tephra emitted by the late period of activity of the YTT resulted in the deposition of thick ignimbrite sequences across 30,000 km^2 of Sumatra (Costa et al., 2014), and that roughly half of this surface is drained toward the Andaman Sea, then about 52 x 10^9 mol/yr of alkalinity are transferred to the Andaman sea through the on-land weathering of the lately emitted YTT.

Would we want to be more precise as to the quantification of the elemental fluxes, we could apply stoechiometric ratios between the chemical compositions of Java basalts (that were considered in the study of "basaltic rivers") and those of the YTT, even if, as demonstrated earlier, this stoichiometric approportionation is not verified in experimental studies of basalt vs rhyolites weathering, and applies even less at the scale of a watershed. We used the tephrostratigraphic study of Caron et al. (2023), who measured the major and trace element concentrations of the tephra layers. Average CaO, MgO, Na_2O and K_2O contents for the tephra layers are respectively 1.0, 0.12, 3.3% and 4.3%, while Java's basalts considered for the weathering study (Louvat, 1997) have average CaO, MgO, Na_2O and K_2O concentrations of 12, 7.2, 2.5 and 3.1% (Romeur, 1990; average of the basalts with 42-55% SiO_2 and >6% MgO).

Thus, YTT tephra contain 12 times less Ca than Java basalts and 60 times less Mg, while containing 1.4 times more Na and K. If we only take into account these stoechiometric proportions between rhyolitic tephra and basalts, then we infer YTT tephra weathering rates of 0.08, 0.01, 0.94 and 0.2 x 10^6 mol/km^2/yr for respectively Ca, Mg, Na and K. The corresponding alkalinity flux to the nearby seas is then 1.05 x 10^6 mol/km^2/yr, roughly 3 times lower than the previous estimates from Java's basaltic rivers. This is a minimum estimation, as the incongruent weathering of basalt and rhyolites/trachytes seems to favor Ca and Mg release against Na, as previously discussed.

We can also expect that the young, porous, non-stabilized and brittle volcanic material emitted by the YTT could weather at least 10 times faster than older rocks, then increasing this alkalinity flux to about 10 x 10^6 mol/km^2/yr.

We thus propose an estimate of the alkalinity flux through the weathering of the YTT deposited on Sumatra between 1 and 10 x 10^6 mol/km^2/yr, resulting in an annual alkalinity flux of between 15 and 150 x 10^9 mol/yr of alkalinity that would be flushed from the YTT volcano toward the Andaman sea.

But on-land weathering is not the only weathering process that can alkalinize the ocean, and these major element fluxes are also not the only ones that should be accounted for. Indeed, on-land chemical weathering fluxes also bring Fe, Ti, and a multitude of geogenic nutrients that will fertilize the ocean while alkalinizing it (e.g. Gilsason et al., 2006; Jones et al, 2014). But ocean fertilization, and alkalinization, will also occur on shorter timescales during volcanic eruptions through tephra fallout to the ocean surface. The time scale of "active" weathering in the ocean will generally correspond to the sedimentation time of these volcanic particles on the ocean floor, which does not exclude later weathering in the sediment layer being formed. The reduction in atmospheric CO_2 during the fertilization of the ocean by post-eruption volcanic ash fallout is another example of the effect of tephra alteration at sea (e.g. Langmann et al., 2010 et

Longman et al, 2022). However, these alkalinization fluxes have not been estimated here. All these weathering and fertilization processes will occur on land and at sea after volcanic eruptions, and their alkalinizing effects compete with the acidifying effect of the volcanic gases and with the screening/cooling effect within the atmosphere that will lower biologic productivity. The cumulative effect will then depend on the pace and intensity of the volcano activity and on the characteristic time scale of each process.

5. Estimation of the alkalinity flux necessary to increase the pH of the Andaman Sea by 0.05 pH unit

The data show a pH increase anomaly following the volcanic activity. We can observe a difference of ~0.05 pH units between the Andaman Sea pH reconstructed from boron isotopes and the pH reconstructed from ice core pCO_2. We estimated the alkalinity variation of ~250 µmol/kgSW (Fig. 4) leading to an alkalinity flux of 9.97×10^{12} mol, considering the volume of the Andaman Sea (Table S4) calculated using the Excel file CO_2Sys_v3.0_Err (Pierrot et al., 2021).

	Andaman Sea
Area (km^2)	797700
Water depth (km)	0.05
Water volume (km^3)	39885
∆ALK (µmol/kgSW)	250
ALK (µmol)	9.97×10^{18}
ALK (mol)	9.97×10^{12}

Table S4. Estimation of the ALK needed to increase the Andaman Sea surface pH by ~0.05 units.

References

B. Langmann, K. Zaksek, M. Hort, and S. Duggen, 2010. Volcanic ash as fertiliser for the surface ocean. Atmos. Chem. Phys. 10, 3891–3899.

Bonatotzky T., Ottner F., Erlendsson E., Gísladóttir G., 2021. Weathering of tephra and the formation of pedogenic minerals in young Andosols, South East Iceland. Catena, 198, doi.org/10.1016/j.catena.2020.105030.

Carey A.E., Mendoza J.A., Welch K.A., Gardner C.B., Goldsmith S.T., Lyons W.B., 2015. Assessment of stream geochemistry in west central Nicaragua during baseflow conditions. Appl. Geochem., 63, 519–526.

Caron, B., Del Manzo, G., Villemant, B., Bartolini, A., Moreno, E., Le Friant, A., Bassinot, F., Baudin, F., Alves, A., 2023. Marine records reveal multiple phases of Toba's last volcanic activity. Sci Rep 13, 11575. https://doi.org/10.1038/s41598-023-37999-w

Chadwick O. A., Derry L. A., Vitousek P. M., Huebert B. J., and Hedin L. O.,1999. Changing sources of nutrients during four million years of ecosystem development. Nature, 397, 491–497

Costa A., Smith V.C., Macedonio G., Matthews N.E., 2014, The magnitude and impact of the Youngest Toba Tuff super-eruption. Front. Earth Sci, doi.org/10.3389/feart.2014.00016

Dahlgren R. A., Ugolini F. C., Casey W. H., 1999. Field weathering rates of Mt. St. Helens tephra. Geochim. Cosmochim. Acta 63, 587–598.

De La Vega, E., Chalk, T.B., Hain, M.P., Wilding, M.R., Casey, D., Gledhill, R., Luo, C., Wilson, P.A., Foster, G.L., 2023. Orbital CO2 reconstruction using boron isotopes during the late Pleistocene, an assessment of accuracy (preprint). Proxy Use-Development-Validation/Marine Archives/Pleistocene. https://doi.org/10.5194/cp-2022-93

Dessert C., Dupré B., François L.M., Schott J., Gaillardet J., Chakrapani G., Bajpai S., 2001. Erosion of Deccan Traps determined by river geochemistry: Impact on the global climate and the 87Sr/86Sr ratio of seawater. Earth Planet. Sci. Lett., 188, 459–474.

Dessert C., Lajeunesse E., Lloret E., Clergue C., Crispi O., Gorge C., Quidelleur X., 2015. Controls on chemical weathering on a mountainous volcanic tropical island: Guadeloupe (French West Indies). Geochim. Cosmochim. Acta, 171, 216-237.

Dessert, C., Gaillardet, J., Dupre, B., Schott, J., Pokrovsky, O.S., 2009. Fluxes of high- versus low-temperature water–rock interactions in aerial volcanic areas: example from the Kamchatka Peninsula, Russia. Geochim. Cosmochim. Acta 73, 148–169.

Eiriksdottir E. S., Gislason S. R. and Oelkers E. H., 2013. Does temperature or runoff control the feedback between chemical denudation and climate? Insights from NE Iceland. Geochim. Cosmochim. Acta 107, 65–81.

Eiriksdottir E. S., Gislason S. R. and Oelkers E. H., 2015. Direct evidence of the feedback between climate and nutrient, major, and trace element transport to the oceans. Geochim. Cosmochim. Acta 166, 249–266.

Eiriksdottir E.S., Louvat P., Gislason S.R., Óskarsson N., Hardardóttir J., 2008, Temporal variation of chemical and mechanical weathering in NE Iceland: Evaluation of a steady-state model of erosion, Earth Planet. Sci. Lett., 272, 78-88.

Gaillardet J., Rad S., Rivé K., Louvat P., Gorge C., Allègre C.J., Lajeunesse R., 2011 Orography- driven chemical denudation in the Lesser Antilles: Evidence for a new feedback mechanism stabilizing atmospheric CO2. Am. J. Sci., 311, 851–894.

Gislason S. R., Eugster H.P., 1987, Meteoric water-basalt interactions. II: A field study in NE. Iceland. Geochim. Cosmochim. Acta, 51, 2841–2855.

Gislason S.R., Arnorsson S., Armannsson H., 1996, Chemical weathering of basalt in SW Iceland: effects of runoff, age of rocks and vegetative/glacial cover: American Journal of Science, v. 296, p. 837–907.

Gislason S.R., Oelkers E.H., Eiriksdottir E.S., Kardjilov M.I., Gisladottir G., Sigfusson B., Snorrason A., Elefsen S.O., Hardardottir J., Torssander P., Oskarsson N., 2009. Direct evidence of the feedback between climate and weathering. Earth Planet. Sci. Lett. 277, 213–222.

Gislason S.R., Oelkers E.H., Snorrason Á., 2006. Role of river-suspended material in the global carbon cycle. Geology 34, 49–52.

Goldsmith S.T., Carey A.E., Johnson B.M., Welch S.A., Lyons W.B., McDowell W.H., Pigott J.S., 2010. Stream geochemistry, chemical weathering and CO2 consumption potential of andesitic terrains, Dominica, Lesser Antilles. Geochim. Cosmochim. Acta, 74, 85–103.

Goldsmith S.T., Carey A.E., Lyons W.B., Hicks D.M., 2008. Geochemical yields and weathering of volcanic terrains on high standing islands: Taranaki and Manawatu-Wanganui regions of New Zealand. Geochim. Cosmochim. Acta, 72, 2248–2267.

Goldsmith S.T., Harmon R.S., Lyons W.B., Harmon B.A., Ogden F.O., Gardner C.B., 2015. Evaluation of controls on silicate weathering in tropical mountainous rivers: Insights from the Isthmus of Panama. Geology, v. 43, p. 563–566.

Guillermic, M., Misra, S., Eagle, R., Villa, A., Chang, F., Tripati, A., 2020. Seawater pH reconstruction using boron isotopes in multiple planktonic foraminifera species with different depth habitats and their potential to constrain pH and CO2 gradients. Biogeosciences 17, 3487–3510. https://doi.org/10.5194/bg-17-3487-2020

Gutjahr, M., Ridgwell, A., Sexton, P.F., Anagnostou, E., Pearson, P.N., Pälike, H., Norris, R.D., Thomas, E., Foster, G.L., 2017. Very large release of mostly volcanic carbon during the Palaeocene–Eocene Thermal Maximum. Nature 548, 573–577. https://doi.org/10.1038/nature23646

Harmon R.S., Wörner G., Goldsmith S.T., Harmon B.A., Gardner C.B., Lyons W.B., Ogden F.L., Pribil M.J., Long D.T., Kern Z., Fórizs I., 2016. Linking silicate weathering to riverine geochemistry—A case study from a mountainous tropical setting in west-central Panama. GSA Bulletin, 128, 1780-1812.

Henehan, M.J., Rae, J.W.B., Foster, G.L., Erez, J., Prentice, K.C., Kucera, M., Bostock, H.C., Martínez-Botí, M.A., Milton, J.A., Wilson, P.A., Marshall, B.J., Elliott, T., 2013. Calibration of the boron isotope proxy in the planktonic foraminifera Globigerinoides ruber for use in palaeo-CO2 reconstruction. Earth and Planetary Science Letters 364, 111–122. https://doi.org/10.1016/j.epsl.2012.12.029

Jones M.T., Gislason S.R., Kevin W. Burton K.W., Pearce C.R., Mavromatis V., von Strandmann P.A.E., Oelkers E.H., 2014. Quantifying the impact of riverine particulate dissolution in seawater on ocean chemistry. EPSL 395, 91-100

Jones M.T., Hembury D.J., Palmer M.R., Tonge B., Darling W.G., Loughlin S.C., 2011. The weathering and element yields from active volcanoes to the oceans: A Monserrat case study. Bull. Volcanol., 73, 207–222.

Jones, M.T., Hembury, D.J., Palmer, M.R., Tonge, B., Darling, W.G., Loughlin, S.C.T., 2011. The weathering and element fluxes from active volcanoes to the oceans: a Montserrat case study. Bulletin of Volcanology 73, 207e222.

Kotov, S., Pälike, H., 2018. QAnalySeries – a cross-platform time series tuning and analysis tool (other). Geology. https://doi.org/10.1002/essoar.10500226.1

Lemarchand, E., Schott, J., Gaillardet, J., 2007. How surface complexes impact boron isotope fractionation: Evidence from Fe and Mn oxides sorption experiments. Earth and Planetary Science Letters 260, 277–296. https://doi.org/10.1016/j.epsl.2007.05.039

Lemelle, L., Bartolini, A., Simionovici, A., Tucoulou, R., De Nolf, W., Bassinot, F., De Garidel-Thoron, T., 2020. Nanoscale trace metal imprinting of biocalcification of planktic foraminifers by Toba's super-eruption. Sci Rep 10, 10974. https://doi.org/10.1038/s41598-020-67481-w

Li G., Hartmann J., Derry L.A., West A.J., You C.F., Long X.Y., Zhan T., Li L.F., Li G., Qiu W.H., Li T., Liu L.W., Chen Y., Ji J. F., Zhao L., Chen J., 2016. Temperature dependence of basalt weathering. Earth Planet. Sci. Lett. 443, 59–69.

Lisiecki, L.E., Stern, J.V., 2016. Regional and global benthic δ^{18}O stacks for the last glacial cycle: Last Glacial Cycle Benthic δ^{18}O. Paleoceanography 31, 1368–1394. https://doi.org/10.1002/2016PA003002

Louvat P., 1997. Etude géochimique de l'érosion fluviale d'îles volcaniques à l'aide des bilans d'éléments majeurs et traces. Thèse, Institut de Physique du Globe. 322p.

Louvat P., Allègre C. J., 1998, Riverine erosion rates on Sao Miguel volcanic island, Azores archipelago. Chem. Geol., 148, 177-200.

Martin, P.A., Lea, D.W., 2002. A simple evaluation of cleaning procedures on fossil benthic foraminiferal Mg/Ca. Geochem.-Geophys.-Geosyst. 3, 1–8. https://doi.org/10.1029/2001GC000280

Olsson-Francis K., Simpson A.E., Wolff-Boenisch D., Cockell C.S., 2014. The effect of rock composition on cyanobacterial weathering of crystalline basalt and rhyolite. Geobiology 10, 434-444.

Pang, X., Bassinot, F., Sepulcre, S., 2021. Indonesian Throughflow variability over the last two glacial-interglacial cycles: Evidence from the eastern Indian Ocean. Quaternary Science Reviews 256, 106839. https://doi.org/10.1016/j.quascirev.2021.106839

Pierrot, D., Epitalon, J.-M., Orr, J.C., Lewis, E., and Wallace, D. W. R., MS Excel program developed for CO2 system calculations – version 3.0, (2021), GitHub repository, https://github.com/dpierrot/co2sys_xl

Rad S., Rivé K., Vittecoq B., Cerdan O., Allègre C.J., 2013. Chemical weathering and erosion rates in the Lesser Antilles: An overview in Guadeloupe, Martinique and Dominica. J. South Am. Earth Sci., 45: 331-344.

Rad S.D., Allègre C. J., Louvat P., 2007. Hidden erosion on volcanic islands. Earth Planet. Sci. Lett., 262, 109 – 124.

Rad S.D., Louvat P., Gorge C., Gaillardet J., Allègre C.J., 2006. River dissolved and solid loads in the Lesser Antilles: new insight into basalt weathering processes. J. Geochem. Explor 88, 308-312.

Rae, J.W.B., Foster, G.L., Schmidt, D.N., Elliott, T., 2011. Boron isotopes and B/Ca in benthic foraminifera: Proxies for the deep ocean carbonate system. Earth and Planetary Science Letters 302, 403–413. https://doi.org/10.1016/j.epsl.2010.12.034

Raitzsch, M., Bijma, J., Benthien, A., Richter, K.-U., Steinhoefel, G., Kučera, M., 2018. Boron isotope-based seasonal paleo-pH reconstruction for the Southeast Atlantic – A multispecies approach using habitat preference of planktonic foraminifera. Earth and Planetary Science Letters 487, 138–150. https://doi.org/10.1016/j.epsl.2018.02.002

Romeur M., 1991. Séries magmatiques arc et arrière-arc de la Sonde : nature des sources impliquées (éléments en trace et isotopes Sr-Nd-Pb). Thèse Université de Brest, France.

Romeur, M.; Dosso, Laure; Maury, R.; Bougault, H.; Joron, J. L., 1990. Arc and back-arc geochemical features of the Sunda Arc; trace element and isotopic (Sr, Nd, Pb) data from South Sumatra, central and East Java. Eos, 71, Issue 43, pp. 1700 (abstract AGU).

Schopka H.H., Derry L.A., 2012. Chemical weathering fluxes from volcanic islands and the importance of groundwater: The Hawaiian example. Earth Planet. Sci. Lett. 339-340, 67–78.

Schopka H.H., Derry L.A., Arcilla C.A., 2011. Chemical weathering, river geochemistry and atmospheric carbon yields from volcanic and ultramafic regions on Luzon Island, the Philippines. Geochim. Cosmochim. Acta 75, 978–1002.

Stewart B.W., Capo R.C., Chadwick O.A., 2001. Effects of rainfall on weathering rate, base cation provenance, and Sr isotope composition of Hawaiian soils. Geochim. Cosmochim. Acta, 65, 1087-1099.

van der Kaars, S., Williams, M.A.J., Bassinot, F., Guichard, F., Moreno, E., Dewilde, F., Cook, E.J., 2012. The influence of the ~73 ka Toba super-eruption on the ecosystems of northern Sumatra as recorded in marine core BAR94-25. Quaternary International 258, 45–53. https://doi.org/10.1016/j.quaint.2011.09.006